

# UDHF<sup>2</sup>-Net: An Uncertainty-diffusion-model-based High-Frequency TransFormer Network for High-accuracy Interpretation of Remotely Sensed Imagery

Pengfei Zhang<sup>a</sup>, Chang Li<sup>a\*</sup>, Yongjun Zhang<sup>b</sup> and Rongjun Qin<sup>c</sup>

<sup>a</sup> *Key Laboratory for Geographical Process Analysis & Simulation of Hubei Province, and College of Urban and Environmental Science, Central China Normal University, Wuhan, China;*

<sup>b</sup> *School of Remote Sensing and Information Engineering, Wuhan University, China.*

<sup>c</sup> *Department of Civil, Environmental and Geodetic Engineering; Department of Electrical and Computer Engineering; Translational Data Analytics Institute, The Ohio State University, Columbus, Ohio, United States of America*

\* Corresponding author: Chang Li, [lcshaka@126.com](mailto:lcshaka@126.com) && [lichang@ccnu.edu.cn](mailto:lichang@ccnu.edu.cn)

## Abstract:

Remotely sensed image high-accuracy interpretation (RSIHI), including tasks such as semantic segmentation and change detection, faces the three major problems: (1) complementarity problem of spatially stationary-and-non-stationary frequency; (2) edge uncertainty problem caused by down-sampling in the encoder step and intrinsic edge noises; and (3) false detection problem caused by imagery registration error in change detection. To solve the aforementioned problems, an uncertainty-diffusion-model-based high-Frequency TransFormer network (UDHF<sup>2</sup>-Net) is proposed for RSIHI, the superiority of which is as following: (1) a spatially-stationary-and-non-stationary high-frequency connection paradigm (SHCP) is proposed to enhance the interaction of spatially stationary and non-stationary frequency features to yield high-fidelity edge extraction result. Inspired by HRFormer, SHCP remains the high-frequency stream through the whole encoder-decoder process with parallel high-to-low frequency streams and reduces the edge loss by a downsampling operation; (2) a mask-and-geo-knowledge-based uncertainty diffusion module (MUDM) is proposed to improve the robustness and edge noise resistance. MUDM could further optimize the

uncertain region to improve edge extraction result by gradually removing the multiple geo-knowledge-based noises; (3) a semi-pseudo-Siamese UDHF<sup>2</sup>-Net for change detection task is proposed to reduce the pseudo change by registration error. It adopts semi-pseudo-Siamese architecture to extract above complemental frequency features for adaptively reducing registration differencing, and MUDM to recover the uncertain region by gradually reducing the registration error besides above edge noises. Comprehensive experiments were performed demonstrating the superiority of UDHF<sup>2</sup>-Net. In the semantic segmentation task, UDHF<sup>2</sup>-Net achieves the best mIoU values of 89.43% and 85.23% respectively on ISPRS Potsdam and Vaihingen datasets compared with state-of-the-art networks (i.e., FT-UNetFormer, HRFormer). In change detection task, semi-pseudo-Siamese UDHF<sup>2</sup>-Net achieves the best IoU values of 90.64% and 85.79% respectively on WHU building and LEVIR-CD dataset compared with state-of-the-art networks (i.e., P2V-CD, ChangeFormer). Especially ablation experiments indicate the effectiveness of UDHF<sup>2</sup>-Net. In semantic segmentation task, UDHF<sup>2</sup>-Net achieves the improvement gains by 0.52% in mIoU than the network without MUDM, at least by 0.97% in mIoU than the single-branch spatially stationary/non-stationary high-frequency connection paradigm; In change detection task, semi-pseudo-Siamese UDHF<sup>2</sup>-Net achieves the improvement gains by 0.55% in mIoU than the network without MUDM, at least by 0.26% than the single-branch spatially stationary/non-stationary high-frequency connection paradigm, by 2.25% than the module based on difference architecture.

**Keywords:** Remotely sensed image high-accuracy interpretation (RSIHI); semantic segmentation; change detection; Spatially-stationary-and-non-stationary high-frequency connection paradigm (SHCP); Mask-and-geo-knowledge-based uncertainty diffusion module (MUDM); semi-pseudo-Siamese UDHF<sup>2</sup>-Net

## 1. Introduction

Remotely sensed image high-accuracy interpretation (RSIHI) is a significant foundation for research aimed at utilizing physical mechanisms to recognize land

surface information and further realize high-accuracy planetary observation from remote sensing images (Li et al., 2019). Particularly it has been successfully used to support a variety of applications, such as food security (Krishnamurthy R et al., 2022; Li et al., 2022c; Tanaka et al., 2023), global climate change (Pascolini-Campbell et al., 2021), sustainable development (Gao and O'Neill, 2020), carbon emissions (Wang et al., 2022a; Yu et al., 2022) and damage assessment (Hantson et al., 2022; Smith et al., 2019; Xu et al., 2022).

Recently the rapid expansion of high-quality remote sensing datasets and the advancement of deep neural network (DNN) have promoted the development of RSIHI toward intelligence, automation and high-accuracy (He et al., 2021; Qi et al., 2020; Shen et al., 2020; Sun et al., 2022; Volpi and Tuia, 2016; Yuan et al., 2020; Zhou et al., 2018). Particularly DNN has demonstrated powerful potential and gradually become the mainstream approach to perform RSIHI. Currently numerous scholars are dedicated to exploring the research of DNN including semantic segmentation and change detection tasks. The two tasks focus on assigning semantic or change labels to each pixel of given remote sensing images to achieve non-dynamic or dynamic analysis of surface information respectively (Bai et al., 2022; Li et al., 2019; Shi et al., 2020).

To effectively understand the complex remote sensing scenes, the popular DNNs concentrate on achieving complex, hierarchical and nonlinear high-dimensional abstract features to perform RSIHI, which are generally divided into three types by different object domains as follows:

(1) Spatial-based DNN. There are three common strategies for extracting effective spatial features to perform RSIHI: local feature extraction, global feature extraction and joint extraction of local and global features. Local feature extraction typically utilizes convolutional neural networks (CNN) to achieve detailed local intricate spatial features using local receptive fields, which may struggle to represent the global spatial relation (Zhang et al., 2020a). In contrast, global feature extraction leverages the Transformer network to capture global context features by its powerful sequence-to-sequence (long-range) relational modelling capability, which is also difficult to represent local spatial

relation (Yang et al., 2023). To bridge the inherent gap between global and local feature extraction, some scholars have adopted the joint extraction strategy of local and global features to complement each other's strengths of CNN and Transformer, which is a balanced and mutually reinforcing strategy for further improving the accuracy of RSIHI (Wang et al., 2022b).

(2) Frequency-based DNN. Some scholars have proposed several frequency-based DNNs to exhibit prominent texture details and improve robustness for scale transformations due to their transformation invariance (Bai et al., 2021; Zheng et al., 2023). In the present studies, several scholars extract spatially stationary frequency features to capture invariant global features(Shan et al., 2021). In contrast, other researchers extract spatially non-stationary frequency features with various scales and positions to capture multiple-scale and local detailed features (Chaudhary et al., 2019). However, there has been no report on the joint spatially stationary-and-non-stationary frequency extraction approach to perform RSIHI. Therefore, this approach holds significant theoretical and methodological exploration value.

(3) Joint frequency-and-spatial DNN. To enhance the richness of the feature extraction, some researchers attempt to fuse frequency and spatial domain features for achieving effective performance (Jia and Yao, 2023). However, it is worth noting that spatial and frequency domain features could be losslessly converted to each other. Therefore, extracting features in two domains simultaneously could increase the computational complexity.

In terms of the accuracy of RSIHI, current literature includes the following problems:

(1) Edge detail distortion is inevitable caused by the downsampling operation in the encoder phase. High-resolution network (HRNet) (Wang et al., 2020) or HRFormer (Yuan et al., 2021) have been proposed as the promising solutions, which preserve a high-resolution stream through the encoder-decoder process to mitigate this issue. However, there is no report on how to deliver high-fidelity edge features for frequency-based DNNs with less edge loss. Specifically, high-frequency features are sensitive to

edge information. Therefore, fully excavating high-frequency features is conducive to improving edge extraction accuracy;

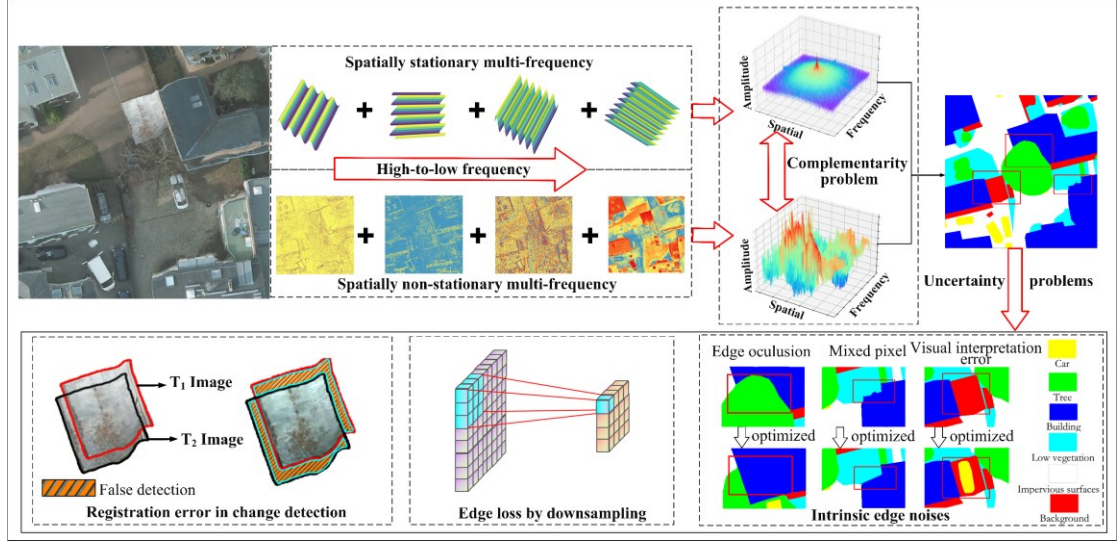


**Figure 1.** The main problems of RSIHI. (1) the complementarity problem of spatially stationary-and-non-stationary frequency; (2) edge uncertainty problem caused by downsampling in encoder step and intrinsic edge noises (i.e., mixed pixels, edge occlusion and visual interpretation error); and (3) false detection problem caused by registration error in change detection.

(2) Edge intrinsic noises are pervasive caused by the following geo-knowledge: mixed pixel (Ball and Wei, 2018; Hong et al., 2021), edge occlusion (Haut et al., 2019; Li et al., 2023; Qiu et al., 2017) and visual interpretation error (Van Coillie et al., 2014).. These noises generally result in location and semantic uncertainty, which can hinder the improvement of edge extraction accuracy. Therefore, it is crucial to consider the denoising ability to enhance the effectiveness of DNNs;

(3) False detection may occur due to registration errors of bi-temporal images in change detection. Imprecise image registration generally could produce the pseudo changes, which leads to higher false detection rates and reduces accuracy of change detection. To our best knowledge, there is currently no related research on frequency-based DNNs to mitigate the effect of registration errors on change detection currently.

To overcome the aforementioned problems, an uncertainty-diffusion-model-based high-Frequency Transformer network (UDHF<sup>2</sup>-Net) is the first to be proposed for performing RSIHI tasks (i.e., semantic segmentation and change detection). The advantages and contributions are as follows:

(1) a spatially-stationary-and-non-stationary high-frequency connection paradigm (SHCP) is proposed to complement each other's advantages of both spatially stationary and non-stationary frequency features. Drawing inspiration from HRFormer (Yuan et al., 2021), SHCP adopts multiple parallel high-to-low frequency streams to improve the ability of feature representation. It also delivers the high-frequency stream to achieve high-fidelity edge details and reduce edge loss due to downsampling operation;

(2) a mask-and-geo-knowledge-based uncertainty diffusion module (MUDM) is proposed to improve the edge extraction robustness and edge noise resistance. Based on the geo-knowledge, the certain region is masked, and the uncertain region could be further optimized to improve edge extraction accuracy by gradually denoising;

(3) a semi-pseudo-Siamese UDHF<sup>2</sup>-Net for change detection task is proposed to reduce the pseudo change by registration error. It adopts semi-pseudo-Siamese architecture to achieve spatially stationary and non-stationary multi-frequency features with original registration differencing, MUDM to adaptively optimize the pseudo change by gradually denoising of registration error besides above edge noises.

## 2. Related work

This section presents a comprehensive review of the literature on RSIHI, with a particular emphasis on semantic segmentation and change detection tasks.

### 2.1 Semantic segmentation

Semantic segmentation is a popular RSIHI task to classify each pixel of an image into a specific category. Three dominant types of DNNs are commonly adopted to enhance capability of feature extraction as follows:

(1) Spatial-based DNN. Current spatial-based DNNs extract deep features from the following perspectives:

1) Local feature extraction. It primarily depends on CNNs to capture fine-grained local intricacies by stacking hierarchical convolutional layers with various local receptive fields (Li et al., 2019), such as Fully Convolutional Networks (Long et al., 2015), UNet (Ronneberger et al., 2015), Deeplab series (Chen et al., 2017; Chen et al., 2018), etc. However, CNNs exhibit evident limitations in its consideration of global

context, which impedes the holistic comprehension of complex remote sensing scenes.

2) Global feature extraction. It relies principally on Transformer network to enable the powerful capability of performing complex sequence-to-sequence (long-range) modelling, such as SegFormer (Xie et al., 2021), Segmenter (Strudel et al., 2021), SwinUNet (Cao et al., 2022a), FT-UNetFormer (Wang et al., 2022a), HRFormer (Yuan et al., 2021), etc.. Additionally, the multi-head attention mechanism is adopted to further obtain contextual information. However, Transformer networks face challenges in recognizing local intricacies, which could prevent them from effectively yielding the local details.

3) Joint extraction of local and global features. To integrate the advantages of local and global features, some DNNs have adopted the hybrid structure of CNN and Transformer to perform the joint extraction strategy of local and global features, which is conducive to complementing each other's strengths (Li et al., 2022a).

In summary, CNN and Transformer demonstrate their remarkable advancements in local and global feature extraction respectively. However, they have their own limitations simultaneously. Therefore, the joint feature extraction strategy provides a successful paradigm to fully maximize their respective advantages for a comprehensive understanding of both intricate local details and complex global information.

(2) Frequency-based DNN. Frequency-based DNN decomposes the image into different frequency components to further represent the structure and texture information. It has witnessed outstanding advancements in the following fields: object detection (Bai et al., 2021; Zheng et al., 2023), image classification (Cao et al., 2022b), image pansharpening (Xing et al., 2023), cloud removal (Guo et al., 2023). Two types of dominant frequency-based DNNs are as follows:

1) Spatially stationary frequency feature extraction. Its primary advantages provide the significant invariant statistical properties that vary with space. That ensures a coherent interpretation of unchanging features and is beneficial to capturing global spectrum information, such as Fourier transform (Jia and Yao, 2023), fast Fourier transform (Shan et al., 2021). However, it generally neglects the sensitivity in detecting

edges within images that undergo significant and abrupt changes;

2) Spatially non-stationary frequency feature representation. Its prominent superiority lies in its ability of capturing statistical properties of significant changes across different regions, such as discrete wavelet transform (Xing et al., 2023), short-time Fourier transform (Chaudhary et al., 2019) and etc. That is beneficial to detecting concentrated or localized features such as edges, textures, and patterns that change over space. However, the approach also encounters challenges in maintaining a coherent global representation.

In addition, Researchers have demonstrated that high-frequency information is beneficial to effectively improving edge extraction accuracy. It carries crucial details related to edges and boundaries (Shan et al., 2021). However, it still faces the dilemma of high-frequency information loss due to the downsampling operation in the encoder process.

In summary, spatially stationary frequency features prove beneficial for handling consistent regions within objects, but it is not sensitive to capture abrupt change information such as edges. Simultaneously, spatially non-stationary frequency features are better suited for addressing edge information, but it is not able to fully express structural information. Importantly, no research has been reported that integrates the above advantages and tackles the aforementioned gaps at the same time. Therefore, the joint extraction of stationarity and non-stationarity frequency features offers a new perspective for constructing an advancing and comprehensive framework to harmonize their complementary strengths.

## **2.2 Change detection task**

Change detection is a prevalent RSIHI task to assign the binary change labels to the paired pixels of bi-temporal images (Cao and Huang, 2023; Wu et al., 2023). Two dominant types of DNNs are shown as follows:

(1) Single-branch architecture. This architecture stacks bi-temporal images by concatenation or difference as the input of DNNs to directly perform classification (Cao and Huang, 2023). The concatenation approach directly stacks bi-temporal images to

extract change information, and the difference method generally adopts image difference to obtain change intensity information (Daudt et al., 2019; Papadomanolaki et al., 2019; Peng et al., 2019). However, this approach could introduce noise owing to registration errors of bi-temporal images. The insufficiency image registration could result in change error accumulation and further reduce the accuracy of change detection (Tian et al., 2022)..

(2) Double-branch architecture. This architecture utilizes two parallel encoders to extract deep features from bi-temporal images separately. The architecture could be categorized into two types: ① Post-Classification network. It could achieve the classification maps of bi-temporal images, and then obtain change map by comparing the differences of the classification maps. It should be noted that the accuracy of change results is directly determined by the effectiveness of the classifier and the image registration errors; ② Siamese network. It could be divided into two types based on whether the weights of the two branches are shared: pseudo-Siamese network with nonshared weights, pure-Siamese network with shared weights and semi-pseudo Siamese network. Several classical networks consist of Changer (Fang et al., 2023), P2V-CD (Lin et al., 2023), ChangeFormer (Bandara and Patel, 2022), etc. Pure-Siamese network could reduce the number of trained parameters and computational complexity, which overlooks the radiation differences of bi-temporal images. And pseudo Siamese network has more flexibility but has the more computational consumption. Different from the above methods, semi-pseudo Siamese network is a balance strategy. It adopts partially shared weights which could share the weights of the previous layers and could not share the weight of the last two or three layers to be trained independently. That could allow the network to adaptively reduce the impact of registration errors and maintain fewer computational parameters.

Summarily, both single-branch and double-branch change detection architectures often emphasize on extract change feature in spatial domain. However, there is a substantial untapped potential in exploring frequency-based change detection networks. Therefore, the frequency-based semi-pseudo-Siamese network could be adopted to

adaptively optimize the registration errors and learn frequency feature representation for capturing change information. To our best knowledge, there are currently no frequency-based change detection DNNs.

Whether in semantic segmentation or change detection tasks, there are several inherent uncertainty in edge as follows: (1) mixed pixel in transition zones easily leads to edge location uncertainty of different objects due to limited resolution (Ball and Wei, 2018; Hong et al., 2021), such as farmland and vegetation, grassland and forest land; (2) edge occlusion generally results in semantic uncertainty (Haut et al., 2019; Li et al., 2023; Qiu et al., 2017). For example, local buildings could be identified as vegetation due to occlusion; (3) visual interpretation error could make different visual interpretation experts to incorrectly label the position and semantic information of the samples, which increase the fitting difficulty of DNN (Lyu et al., 2020; Wu et al., 2021).

Importantly, many scholars have successfully adopted the denoising diffusion probabilistic model to denoise in the field of remote sensing owing to its outstanding denoising performance and robustness, such as image generation (Yuan et al., 2023), cloud removing (Zou et al., 2023). The overarching goal of a diffusion probabilistic model is to generate a Markov chain for achieving random noise into the input data, and then training this Markov chain to employ variational inference to exhibit exceptional performance (Croitoru et al., 2023). It consists of two fundamental stages: the forward diffusion process and the reverse denoising process (Ho et al., 2020). During the forward stage, Gaussian noise is continuously added over multiple time steps for training; In the reverse stage, the original data could be reconstructed by minimizing the discrepancy between the discrepancy between the predicted and added noise gradually.

Existing approaches aims to generate global noise but lack attention to local uncertain regions, especially edge regions.

Summarily, we propose an UDHF<sup>2</sup>-Net to perform effectively RSIHI which could be applied in semantic segmentation and change detection tasks. Our superior solution is demonstrated in the following aspects: (1) We are the first to study how to make the

most of the benefits of spatially stationary and non-stationary features in frequency domain for capturing global and local information simultaneously. Notably, high-frequency features are further explored to deliver lossless edge information for avoiding edge loss due to downsampling in encoder step; (2) We are the first to study how to take fully advantages of denoising diffusion probabilistic model for further reducing edge noise and increasing the robustness of the edge uncertain regions; (3) We are the first to study how to adaptively reduce the registration errors and perform efficiently change information extraction and perform efficiently change information extraction.

### 3. Methodology

UDHF<sup>2</sup>-Net is proposed to perform high-accuracy image interpretation in remote sensing semantic segmentation and change detection tasks. As illustrated in Fig.2, the framework of UDHF<sup>2</sup>-Net is an end-to-end Cascade architecture, which consists of the following main components: (1) Spatially-stationary-and-non-stationary high-frequency connection paradigm (SHCP); (2) Mask-and-geo-knowledge-based uncertainty diffusion module (MUDM). In addition, the semi-pseudo-Siamese UDHF<sup>2</sup>-Net is proposed to perform change detection task.

#### 3.1 *Spatially-stationary-and-non-stationary high-frequency connection paradigm*

As illustrated in Fig.2(b), SHCP adopts the Encoder-Decoder architecture to generate initial segmentation result, which consists of the following parts: (1) symmetric spatially-stationary-and-non-stationary high-frequency Transformer encoder; (2) spatially stationary-and-non-stationary multi-frequency fusion decoder.

##### 3.1.1 *Symmetric spatially-stationary-and-non-stationary high-frequency Transformer encoder*

The proposed encoder has four stages. In the first step, the input image  $\mathbf{X} \in \mathbb{R}^{H \times W \times 3}$  could be transformed to multiple spatially stationary and non-stationary frequency features  $\mathbf{F}_{\text{stationary}}$  and  $\mathbf{F}_{\text{non-stationary}}$  respectively, then they are fed into the symmetric multi-frequency parallel transformer encoder to generate the multiple high-to-low frequency streams.

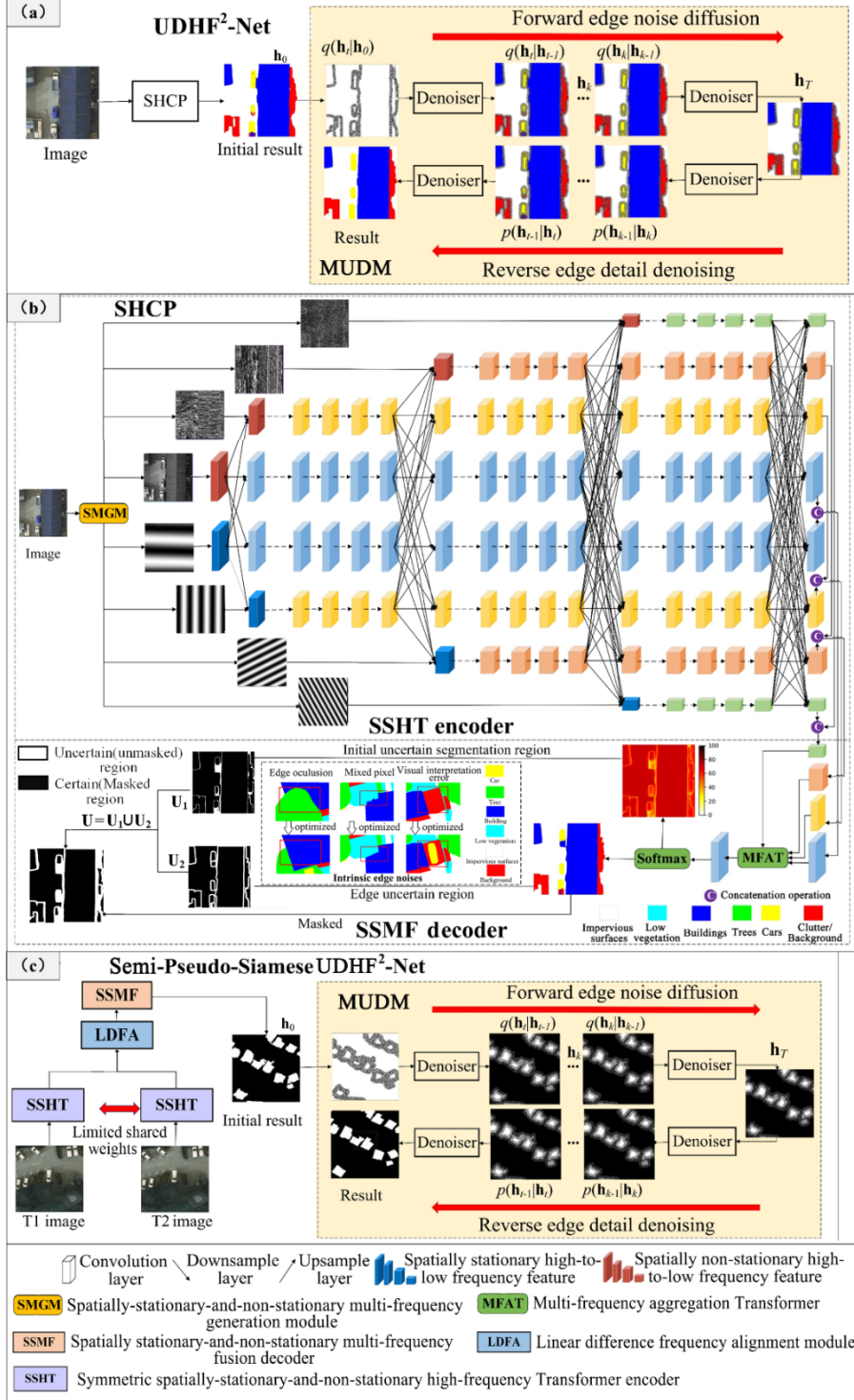


**Figure 2.** Overview of the proposed UDHF<sup>2</sup>-Net. (a) the overall architecture; (b) spatially-stationary-and-non-stationary high-frequency connection paradigm (SHCP); (c) the semi-pseudo-Siamese UDHF<sup>2</sup>-Net for change detection task.

### (1) Spatially-stationary-and-non-stationary multi-frequency generation module

To capture local abrupt change information,  $\mathbf{X}$  could be decomposed into four

spatially non-stationary frequency components based on Discrete Wavelet Transform along the rows and columns with the high-pass filter  $\mathbf{F}_{\text{high}} = [1/\sqrt{2}, -1/\sqrt{2}]$  and the low-pass filter  $\mathbf{F}_{\text{low}} = [1/\sqrt{2}, 1/\sqrt{2}]$ , i.e.,  $\mathbf{F}_{\text{non-stationary}} = [\mathbf{T}_{\text{HH}}, \mathbf{T}_{\text{LH}}, \mathbf{T}_{\text{HL}}, \mathbf{T}_{\text{LL}}]$ . The subband frequency component  $\mathbf{F}_{\text{non-stationary}}^i$  could be arranged from high-frequency to low-frequency as the index  $i \in \{1,2,3,4\}$ .

To capture global consistent information, the input  $\mathbf{X}$  could be decomposed into the multiple high-to-low spatially stationary frequency components with Discrete Fourier Transform, which is shown as Eq.(1):

$$\begin{aligned} \mathbf{F}_{\text{stationary}}(x, y) &= \frac{1}{WH} \sum_{m=0}^{W-1} \sum_{n=0}^{H-1} \mathbf{X}(m, n) e^{-2\pi i(um/W + vn/H)} \\ &= \frac{1}{WH} \sum_{m=0}^{W-1} \sum_{n=0}^{H-1} \mathbf{X}(m, n) (\cos 2\pi um/W - l \sin 2\pi um/W) (\cos 2\pi vn/H - l \sin 2\pi vn/H) \end{aligned} \quad (1)$$

where  $H$  and  $W$  represent the height and width of the input image.  $u$  and  $v$  are the frequency coordinates.  $\mathbf{F}_{\text{stationary}}$  represents the extracted multiple spatially stationary features which includes high-to-low frequency features as the index  $i \in \{1,2,3,4\}$ .

Besides, multiple corresponding stride-2  $3 \times 3$  convolution layers are performed for every frequency component of  $\mathbf{F}_{\text{stationary}}$  and  $\mathbf{F}_{\text{non-stationary}}$  to decrease the resolution to 1/4, 1/8, 1/16, 1/32 of the original resolution respectively from high frequency to low frequency.

## (2) Symmetric multi-frequency parallel Transformer

To enhance the discriminative independently of different frequency features, the symmetric multi-frequency parallel transformer is proposed to improve the above spatially stationary and non-stationary feature representation respectively in every stage. Multi-scale frequency components of  $\mathbf{F}_{\text{stationary}}$  and  $\mathbf{F}_{\text{non-stationary}}$  could be as the input to generate multiple parallel frequency streams to provide fine-grained edge details and coarse-grained structure information. Starting from the first high-frequency stream, each frequency component of  $\mathbf{F}_{\text{stationary}}$  and  $\mathbf{F}_{\text{non-stationary}}$  could be as input and gradually added to the next high-to-low frequency streams over spatially

stationary and non-stationary features in the next stage one by one. It is worth mentioning that the later symmetric frequency streams always consist of all previous higher frequency streams.

### (3) High-frequency Transformer module

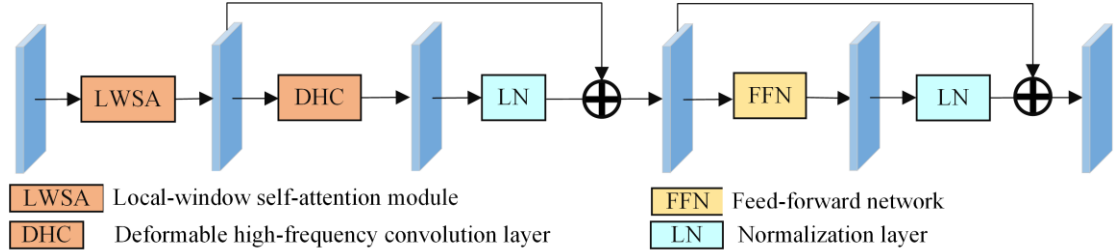


**Figure 3.** Illustration of the high-frequency Transformer module.

In every frequency stream, the proposed high-frequency Transformer module illustrated in Fig.3 is proposed to introduce the deformable convolution for improving the adaptive frequency aggregation ability with larger receptive field. For the input frequency feature  $\mathbf{Z} \in \mathbb{R}^{h \times w \times D}$  of each frequency stream, this proposed module is composed of the following components: (1) Local-window self-attention module. Following formulations in HRFormer (Yuan et al., 2021),  $\mathbf{Z}$  could be divided into a series of non-overlapping local windows of size  $L \times L$ :  $\mathbf{Z} \Rightarrow \{\mathbf{Z}_1, \mathbf{Z}_2, \dots, \mathbf{Z}_n\}$ . Based on local-window self-attention module, the local frequency features of each window are aggregated and merged to generate  $\mathbf{M} \in \mathbb{R}^{h \times w \times E}$ ; (2) Feed-forward network with deformable high-frequency convolution layer is proposed and illustrated by:

$$\mathbf{D} = (\mathbf{M} + \text{LN}(\text{DHC}(\mathbf{M}))) + \text{LN}(\text{FFN}(\mathbf{M} + \text{LN}(\text{DHC}(\mathbf{M})))) \quad (2)$$

where  $\text{DHC}(\cdot)$  denotes deformable high-frequency convolution layer,  $\text{LN}(\cdot)$  denotes the normalization layer,  $\text{FFN}(\cdot)$  denotes Feed-forward network. It is worth mentioning that deformable high-frequency convolution layer could be formulated by (Wang et al., 2023a):

$$\mathbf{D}(r_0) = \sum_{t=1}^T \sum_{n=1}^N (\mathbf{W}_t \mathbf{U}_{tn} \mathbf{M}_t(r_0 + r_n + \Delta r_{tn})) \quad (3)$$

where the input  $\mathbf{M}$  could be sliced into  $T$  groups of feature map  $\mathbf{M}_t \in \mathbb{R}^{h \times w \times E'}$ , and  $E' = E/T$  denotes the channel value of the group.  $\mathbf{W}_t \in \mathbb{R}^{E' \times E}$  and  $\mathbf{U}_{tn} \in \mathbb{R}$  represent the location-irrelevant weight matrix in the  $t$ -th group respectively.  $\mathbf{U}_{tn} \in$

$\mathbb{R}$  could be regarded as the modulation scalar of the  $n$ -th sampling location, which could be normalized by the softmax along the channel  $N$ .  $\Delta r_{tn}$  denotes the offset of the sampling location  $r_n$  of the  $t$ -th group.

#### (4) Cross-frequency connection module

To enhance the interaction and complementarity of multiple spatially stationary and non-stationary frequency features, the cross-frequency connection module is proposed among different stages.

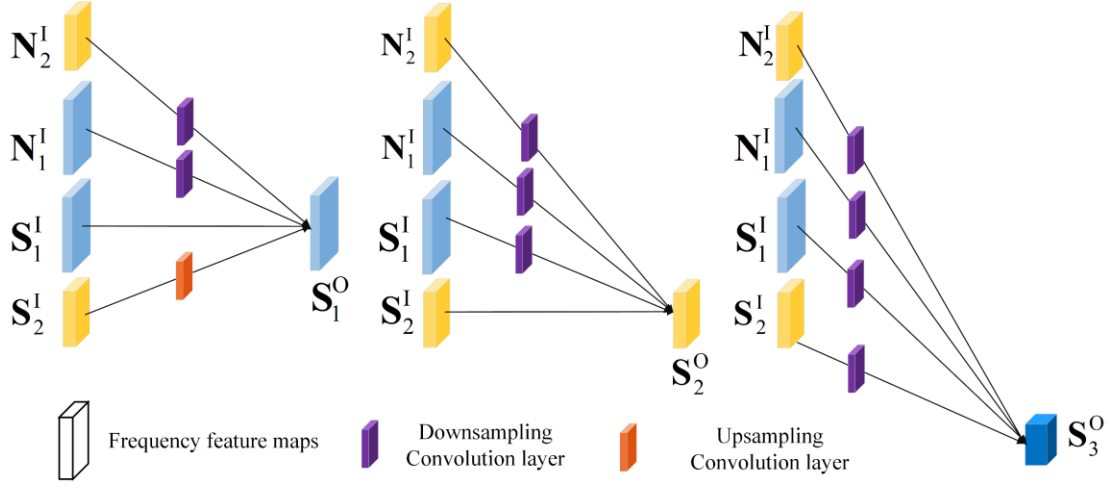


**Figure 4.** Illustration of the cross-frequency connection module.  $\mathbf{N}_k^I$  and  $\mathbf{S}_k^I$  represent input spatially non-stationary and stationary frequency features.  $\mathbf{S}_k^O$  is the output of the spatially stationary frequency feature. And  $k$  represents the frequency index.

For instance, Fig.4 describes how to connect the multiple input spatially non-stationary frequency features  $\{\mathbf{N}_k^I, k = 1,2\}$  and spatially stationary frequency features  $\{\mathbf{S}_k^I, k = 1,2\}$  in details, where  $k$  denotes the frequency index. And the related output features are  $\{\mathbf{S}_k^O, k = 1,2,3\}$ . It is worth mentioning that every output frequency feature could fuse the high-to-low spatially-stationary-and-non-stationary frequency features from the previous stage by:  $\mathbf{S}_k^O = \mathcal{H}_{1k}(\mathbf{N}_1^I) + \mathcal{H}_{2k}(\mathbf{N}_2^I) + \mathcal{H}_{3k}(\mathbf{N}_3^I) + \mathcal{H}_{1k}(\mathbf{S}_1^I) + \mathcal{H}_{2k}(\mathbf{S}_2^I) + \mathcal{H}_{3k}(\mathbf{S}_3^I)$ .

The connection function  $\mathcal{H}_{jk}(\cdot)$  is determined by the input frequency index  $j$ . If  $j = k$ ,  $\mathcal{H}_{jk}(\mathbf{S}) = \mathbf{S}$ ; If  $j < k$ ,  $\mathcal{H}_{jk}(\mathbf{S}) = \text{DWConv}(\mathbf{S})$  where  $\text{DWConv}(\cdot)$  denotes the downsampling operation by the  $(k - j)$  stride-2  $3 \times 3$  convolution layer; If  $j > k$ ,  $\mathcal{H}_{jk}(\mathbf{S}) = \text{UPConv}(\mathbf{S})$  where  $\text{UPConv}(\cdot)$  denotes the  $1 \times 1$  bilinear upsampling

convolution layer and the scale factor is set to  $(k - j)$ ;

### 3.1.2 Spatially stationary-and-non-stationary multi-frequency fusion decoder

As illustrated in Fig.2(b), this decoder is proposed to adaptively align and fuse the above extracted spatially stationary and non-stationary frequency features, and a multi-frequency aggregation Transformer is proposed to gradually enhance the fused frequency features from low frequency to high frequency. The details are described as follows:

Firstly, the obtained spatially stationary and non-stationary multi-frequency features from the proposed encoder, i.e.,  $\mathbf{E}_{\text{stationary}}$  and  $\mathbf{E}_{\text{non-stationary}}$ , are fused by:

$$\mathbf{E}_{\text{fusion}}^i = \text{Cat}(\mathbf{E}_{\text{non-stationary}}^i, \mathbf{E}_{\text{stationary}}^i), i \in \{1, 2, 3, 4\} \quad (4)$$

where  $\mathbf{E}_{\text{fusion}}^i$  and  $\text{Cat}(\cdot)$  denote the  $i$ -th output fused frequency feature and the concatenation operation respectively.

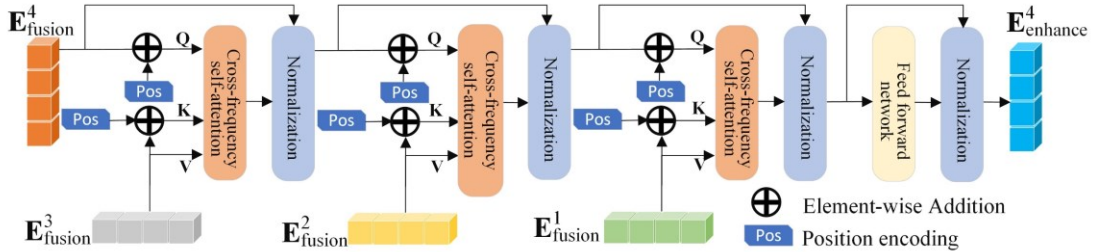


**Figure 5.** Illustration of the multi-frequency aggregation Transformer.

Secondly, the multi-frequency aggregation Transformer is proposed to model high-frequency and low-frequency correlation for enhancing feature representation as shown in Fig.5, aiming at taking the complementary advantage of the edge information in high-frequency features and structural information in low-frequency features. For example,  $\mathbf{E}_{\text{fusion}}^4$  could be strengthened from low frequency to high frequency by gradually fusing  $\mathbf{E}_{\text{fusion}}^3, \mathbf{E}_{\text{fusion}}^2, \mathbf{E}_{\text{fusion}}^1$ , which is described by:

$$\mathbf{E}_{\text{enhance}}^4 = \text{NL} \left( \text{FFN} \left( \text{NL} \left( \text{CS} \left( \text{NL} \left( \text{CS} \left( \text{NL} \left( \text{CS} \left( \mathbf{T}_{\text{fusion}}^4, \mathbf{T}_{\text{fusion}}^3 \right), \mathbf{T}_{\text{fusion}}^2 \right), \mathbf{T}_{\text{fusion}}^1 \right) \right) \right) \right) \right) \right) \quad (5)$$

where  $\mathbf{E}_{\text{enhance}}^1$ ,  $\text{CS}(\cdot)$ ,  $\text{NL}(\cdot)$  and  $\text{FFN}(\cdot)$  represent the enhanced output feature, the cross-frequency self-attention layer, normalization layer and Feed-forward network.

The cross-frequency self-attention layer could be performed by efficient attention

(Zhuoran et al., 2021) to improve multi-frequency interaction. Different frequency features could be projected into tokens with the same size, the input low-frequency features are linearly transformed into **Q** value, the input high-frequency features are linearly transformed into **V** and **K** values. The cross-frequency self-attention layer is leveraged to compute the attention weights for capturing the correlation of different frequency features.

Finally, the fusion features could be gradually enhanced to generate  $\mathbf{E}_{\text{enhance}}^1$ . And a  $4\times$ upsampling convolution layer is added to recover deep features to the original resolution.

### 3.2 Mask-and-geo-knowledge-based uncertainty diffusion module

Although the above proposed SHCP could effectively alleviate the edge detail loss, the inherent uncertainties in the edge still includes the other noises: (1) mixed pixels (Ball and Wei, 2018; Hong et al., 2021); (2) edge occlusion (Haut et al., 2019; Li et al., 2023; Qiu et al., 2017); (3) visual interpretation errors (Van Coillie et al., 2014). Although these uncertainties could not be addressed by the proposed paradigm, they could be regarded as geo-knowledge to further improve the edge extraction accuracy. Therefore, MUDM is proposed as follows:

(1) Masking the certain region by finding the uncertain region. The initial segmentation result of SHCP could be defined as two regions, i.e., the certain and uncertain regions. The uncertain region consists of the following two parts:

① Defining the initial uncertain (unmasked) segmentation region. It is defined by the segmentation probability of SHCP. If the maximum segmentation probabilities of these pixels are lower than a threshold  $\rho$ , these pixels could be set as the uncertain region. The formula is defined by:

$$\mathbf{U}_1 = \begin{cases} 1, & \text{if } \max\left(e^{O_k^1}/\sum_{i=1}^N e^{O_k^i}, \dots, e^{O_k^j}/\sum_{i=1}^N e^{O_k^i}, \dots, e^{O_k^N}/\sum_{i=1}^N e^{O_k^i}\right) \leq \rho \\ 0, & \text{otherwise} \end{cases} \quad (6)$$

Where  $\mathbf{U}_1$  is defined as the initial uncertain segmentation region based on the segmentation probability,  $O_k^j$  is the output of the  $k$ -th pixel from the proposed SHCP for the  $j$ -th category,  $N$  represents the category number,  $\max(\cdot)$  is used to obtain the

maximum probability.

② edge uncertain (masked) region. The initial segmentation label is vectorized by the method of Potrace (Selinger, 2017) to obtain the edge. Then the edge uncertain region is determined to construct a buffer region, i.e.,  $\mathbf{U}_2$ .

The uncertain region  $\mathbf{U}$  and the certain region  $\mathbf{C}$  are obtained by:

$$\begin{aligned}\mathbf{U} &= \mathbf{U}_1 \cup \mathbf{U}_2 \\ \mathbf{C} &= \mathbf{R} - \mathbf{U}\end{aligned}\quad (7)$$

where  $\mathbf{U}$  is defined by obtaining the union of the initial uncertain segmentation region  $\mathbf{U}_1$  and the edge uncertain region  $\mathbf{U}_2$ ,  $\mathbf{C}$  is masked and defined as the certain region by obtaining the complement of  $\mathbf{U}$  in the whole region of the initial segmentation label, i.e.,  $\mathbf{R}$ .

Importantly, the certain region of the initial segmentation label is masked to preserve the original result, while the uncertain (unmasked) region could be further optimized by the proposed MUDM.

(2) Adding training noise by geo-knowledge. Two strategies of data augmentation are proposed to improve the noise resistance as follows: ① edge mixed pixel augmentation. In the uncertain region, the mixed pixel  $M^n$  for the  $n$ -th band of image (e.g.,  $n \in [1,4]$ ) could be constructed from three samples  $M_i^n$ ,  $M_j^n$  and  $M_k^n$  of different classes:

$$M^n = \alpha M_i^n + \beta M_j^n + (1 - \alpha - \beta) M_k^n, \text{ s.t. } 0 \leq \alpha, \beta \leq 1 \quad (8)$$

where  $\alpha$ ,  $\beta$  are the weights.  $M_i^n$ ,  $M_j^n$  and  $M_k^n$  respectively represent the random pixels of the  $i$ -th,  $j$ -th and  $k$ -th class which respectively represent impervious surfaces, buildings and clutter/background in ISPRS Vaihingen and Potsdam datasets; ② edge occlusion sample augmentation. The incorrect occlusion labels are corrected and massive simulated occlusion samples are generated. Occlusion samples are chosen and randomly located in the range of the uncertainty edge regions to overlay on the occluded samples to increase the variability of samples.

(3) Optimizing the uncertain segmentation with MUDM. MUDM is proposed to optimize the above uncertain regions, which consists of the following two processes:

In the forward edge noise diffusion process, MUDM is leveraged to train a Markovian noising process  $q$  to generate a series of noisy data from  $\mathbf{h}_0$  to  $\mathbf{h}_T$  in the uncertain region of the initial segmentation  $\mathbf{h}_0$ . It gradually adds the geo-knowledge-based noise to data distribution  $q(\mathbf{h}_0)$  over a finite iteration  $T$  based on a variance schedule  $\mu_1, \dots, \mu_T$ , which could be formulated by:

$$\begin{aligned} q(\mathbf{h}_{1:T}|\mathbf{h}_0) &= \prod_{t=1}^T q(\mathbf{h}_t|\mathbf{h}_{t-1}) \\ q(\mathbf{h}_t|\mathbf{h}_{t-1}) &= \mathcal{N}(\mathbf{h}_t; \sqrt{1-\mu_t}\mathbf{h}_{t-1}, \mu_t \mathbf{I}) \end{aligned} \quad (9)$$

where  $\mathcal{N}(\cdot; \cdot)$  satisfies the Gaussian distribution,  $\mu_t \mathbf{I}$  and  $\mathbf{I}$  represent the variance matrix and the identity matrix. standard normal distribution. And the direct data distribution  $q(\mathbf{h}_t|\mathbf{h}_0)$  from  $\mathbf{h}_0$  to  $\mathbf{h}_t$  could be derived by:

$$q(\mathbf{h}_t|\mathbf{h}_0) = \mathcal{N}(\mathbf{h}_t; \sqrt{\gamma_t}\mathbf{h}_0, (1-\gamma_t)\mathbf{I}) = \sqrt{\gamma_t}\mathbf{h}_0 + \sqrt{1-\gamma_t}\boldsymbol{\varphi}, \boldsymbol{\varphi} \sim \mathcal{N}(0, \mathbf{I}) \quad (10)$$

where  $\gamma_t = 1 - \mu_t$  and  $\gamma_t = \prod_{k=1}^t \gamma_k$ , and  $\boldsymbol{\varphi}$  indicates random noise from a Gaussian distribution in semantic segmentation.

In the reverse edge detail denoising process, MUDM aims at leveraging the denoiser to gradually denoise the image  $\mathbf{h}_t$  to optimize the uncertain region and obtain  $\mathbf{h}_{t-1}$ . The proposed SHCP is chosen as denoiser to parameterize the reverse distribution. It is performed by:

$$p_\theta(\mathbf{h}_{t-1}|\mathbf{h}_t) := \mathcal{N}(\mathbf{h}_{t-1}; \nu_\theta(\mathbf{h}_t, t), \Sigma_\theta(\mathbf{h}_t, t)) \quad (11)$$

where  $t \in [1, T]$ ,  $\nu_\theta$  and  $\Sigma_\theta$  represent the mean and variance of the prior distribution segmented by the model.

### 3.3 Semi-Pseudo-Siamese UDHF<sup>2</sup>-Net for change detection task

Semi-pseudo-Siamese UDHF<sup>2</sup>-Net is proposed to further reduce pseudo change caused by image registration errors of bi-temporal images for change detection task. It consists of the following two stages:

#### (1) Obtaining initial changed label

In the decoder phase, the semi-pseudo-Siamese architecture with partially shared weights is adopted as the encoder for the input of  $\mathbf{X}_1 \in \mathbb{R}^{H \times W \times 3}$  and  $\mathbf{X}_2 \in \mathbb{R}^{H \times W \times 3}$ . It is beneficial to independently extract spatially-stationary-and-non-stationary high-to-low frequency features from bi-temporal images by:

$$(\mathbf{P}_{\text{stationary}}, \mathbf{P}_{\text{no-stationary}}), (\mathbf{Q}_{\text{stationary}}, \mathbf{Q}_{\text{no-stationary}}) = \text{SSHT}(\mathbf{X}_1), \text{SSHT}(\mathbf{X}_2) \quad (12)$$

where  $\mathbf{P}_{\text{stationary}}$  and  $\mathbf{P}_{\text{no-stationary}}$  denote the output multiple spatially stationary frequency features of  $\mathbf{X}_1$  and  $\mathbf{X}_2$ ,  $\mathbf{Q}_{\text{stationary}}$  and  $\mathbf{Q}_{\text{no-stationary}}$  denote the output multiple spatially non-stationary frequency features of  $\mathbf{X}_1$  and  $\mathbf{X}_2$ ,  $\text{SSHT}(\cdot)$  represents the proposed symmetric spatially-stationary-and-non-stationary high-frequency Transformer in section 3.1.1. Different from the pseudo-Siamese architecture, the semi-pseudo-Siamese architecture has shared some parameters and remains the last two layers to train independently, which are leveraged to reduce computational memory.

To adaptively align difference features of multiple frequency features, a linear difference frequency alignment module is proposed by:

$$\begin{aligned} \mathbf{R}_{\text{stationary}}^i &= \text{BN} \left( \text{Relu} \left( \text{Conv} \left( \text{Cat}(\mathbf{P}_{\text{stationary}}^i, \mathbf{Q}_{\text{stationary}}^i) \right) \right) \right) \\ \mathbf{R}_{\text{non-stationary}}^i &= \text{BN} \left( \text{Relu} \left( \text{Conv} \left( \text{Cat}(\mathbf{P}_{\text{non-stationary}}^i, \mathbf{Q}_{\text{non-stationary}}^i) \right) \right) \right) \end{aligned} \quad (13)$$

where  $\text{Cat}(\cdot)$ ,  $\text{Relu}(\cdot)$ ,  $\text{Conv}(\cdot)$ ,  $\text{Relu}(\cdot)$ ,  $\text{BN}(\cdot)$ ,  $\mathbf{R}_{\text{non-stationary}}^i$ ,  $\mathbf{R}_{\text{stationary}}^i$  denote the concat operation, Relu activation function,  $1 \times 1$  convolution layer, batch normalization layer, the  $i$ -th output of spatially non-stationary frequency features and the  $i$ -th output of spatially stationary frequency features respectively.

In decoder phase, the proposed spatially stationary-and-non-stationary multi-frequency fusion decoder is chosen as the decoder to enhance the complementarity by:

$$\mathbf{R} = \text{SSMF}(\mathbf{F}_{\text{non-stationary}}, \mathbf{F}_{\text{stationary}}) \quad (14)$$

where  $\mathbf{R}$  is the output of the initial change label and  $\text{SSMF}(\cdot)$  represents the spatially stationary-and-non-stationary multi-frequency fusion decoder in subsection 3.1.2.

## (2) Optimizing uncertain region

The proposed MUDM is also adopted to optimize the initial change result. It consists of the following parts:

① Masking the certain region by finding the uncertain region. Based on the above obtained initial change label, the certain region is masked to remain the original result,

and the rest is regarded as the uncertain (unmasked) region. The detailed description is shown in section 3.2.

② Adding training noise by geo-knowledge. Apart from the aforementioned geo-knowledge uncertainty in section 3.2, the registration error of bi-temporal images is simulated in the uncertain region by:

$$\begin{aligned}\dot{x} &= a_0 + \Delta a_0 + (a_1 + \Delta a_1)x + (a_2 + \Delta a_2)y \\ \dot{y} &= b_0 + \Delta b_0 + (b_1 + \Delta b_1)x + (b_2 + \Delta b_2)y\end{aligned}\quad (15)$$

where  $x$  and  $y$  represent the coordinate of the image on time phase 2,  $\dot{x}$  and  $\dot{y}$  represents the simulated coordinate of the image on time phase 2 with random registration error,  $a_0, a_1, a_2, b_0, b_1, b_2$  are the random correction coefficients, where  $\Delta a_0, \Delta b_0 \in [-1.5, 1.5]$ ; and  $|\Delta a_1|, |\Delta a_2|, |\Delta b_1|, |\Delta b_2| \in [10^{-3}, 10^{-5}]$ .

③ Optimizing the uncertain change with uncertainty diffusion model. The uncertain region of the initial change segmentation result is optimized by uncertainty diffusion model to improve the edge extraction accuracy.

### 3.4 Loss function

#### 3.4.1 Loss function for semantic segmentation task

The two-stage cascade loss is leveraged to optimize the proposed UDHF<sup>2</sup>-Net in semantic segmentation task.

In the first stage, a hybrid loss  $\mathcal{L}_{\text{seg}}$  is applied to train the proposed SHCP for achieving the initial segmentation result, which consists of a dice loss  $\mathcal{L}_{\text{dice}}$  and a cross-entropy loss  $\mathcal{L}_{\text{ce}}$ . It could be formulated as by:

$$\begin{aligned}\mathcal{L}_{\text{seg}} &= \gamma \mathcal{L}_{\text{ce}} + (1 - \gamma) \mathcal{L}_{\text{dice}} \\ \mathcal{L}_{\text{ce}} &= -(\sum_{n=1}^N \sum_{c=1}^C (y^{c,n} \log \hat{y}^{c,n})) / N \\ \mathcal{L}_{\text{dice}} &= 1 - 2(\sum_{n=1}^N \sum_{c=1}^C (y^{c,n} \hat{y}^{c,n} / (y^{c,n} + \hat{y}^{c,n}))) / N\end{aligned}\quad (16)$$

where  $\gamma \in [0, 1]$  is the weighted coefficient,  $C$  is the number of classes and  $N$  is the total number of pixels in the image.  $y$  represents the one-hot encoding of the truth label.  $\hat{y}$  is the output predicted probability of the SHCP.

In the second stage, the uncertain loss  $\mathcal{L}_{\text{uncertain}}$  is leveraged to optimize the uncertain region of the initial segmentation result, which consists of an edge uncertainty loss  $\mathcal{L}_{\text{Eu}}$  and a diffusion loss  $\mathcal{L}_{\text{diff}}$  by:

$$\begin{aligned}
\mathcal{L}_{\text{uncertain}} &= \omega \mathcal{L}_{\text{diff}} + (1 - \omega) \mathcal{L}_{\text{Eu}} \\
\mathcal{L}_{\text{diff}} &= \mathbb{E}_{t, \mathbf{h}_0, \varphi} [\| \boldsymbol{\varphi}_{\text{seg}} - \boldsymbol{\varphi}_{\text{seg}}^\theta (\sqrt{\mu_t} \mathbf{h}_0 + \sqrt{1 - \mu_t} \boldsymbol{\varphi}_t) \|^2] \\
\mathcal{L}_{\text{Eu}} &= 1 - 2 \times \text{Precison}_{\text{seg}} \times \text{Recall}_{\text{seg}} / (\text{Precison}_{\text{seg}} + \text{Recall}_{\text{seg}})
\end{aligned} \tag{17}$$

where  $\omega \in [0,1]$  is the weighted coefficient,  $\boldsymbol{\varphi}_{\text{seg}}^\theta$  indicates the parameterized denoiser,  $\boldsymbol{\varphi}_{\text{seg}} \sim \mathcal{N}(0, \mathbf{I})$  indicates random noise from a Gaussian distribution in semantic segmentation, and  $\mathbf{h}_0$  represents the initial segmentation result.  $\boldsymbol{\varphi}_t$  is a function approximator aimed to predict  $\boldsymbol{\varphi}$  from  $\mathbf{h}_t$ .  $\text{Precison}_{\text{seg}}$  and  $\text{Recall}_{\text{seg}}$  are the precision and recall values to evaluate the truth label and predicted label in the uncertain region.

### 3.4.2 Loss function for change detection task

The two-stage cascade loss is used to optimize the proposed semi-pseudo-Siamese UDHF<sup>2</sup>-Net in change detection task.

In the first stage, the hybrid loss  $\mathcal{L}_{\text{cd}}$  is chosen to optimize the initial change result, which consists of a weighted cross entropy loss  $\ell_{\text{wbce}}$  and a dice loss  $\ell_{\text{dice}}$  by:

$$\begin{aligned}
\ell_{\text{cd}} &= g \ell_{\text{wbce}} + (1 - g) \ell_{\text{dice}} \\
\ell_{\text{wbce}} &= -(\lambda \varrho \log(\hat{\varrho}) + (1 - \lambda)(1 - \varrho) \log(1 - \hat{\varrho})) \\
\ell_{\text{dice}} &= 1 - 2\varrho\hat{\varrho}/(\varrho + \hat{\varrho})
\end{aligned} \tag{18}$$

where  $g, \lambda \in [0,1]$  is the weighted coefficient,  $\varrho_i$  represents the truth label and  $\hat{\varrho}$  is the predicted probability.

In the second stage, the uncertain loss  $\ell_{\text{uncertain}}$  is chosen to optimize the uncertain region of the initial change result, which consists of an edge uncertainty loss  $\ell_{\text{Eu}}$  and a diffusion loss  $\ell_{\text{diff}}$  by:

$$\begin{aligned}
\ell_{\text{uncertain}} &= \lambda \ell_{\text{diff}} + (1 - \lambda) \ell_{\text{Eu}} \\
\ell_{\text{diff}} &:= \mathbb{E}_{t, \mathbf{Y}_0, \psi} [\| \boldsymbol{\varphi}_{\text{cd}} - \boldsymbol{\varphi}_{\text{cd}}^\theta (\sqrt{\mu_t} \mathbf{Y}_0 + \sqrt{1 - \mu_t} \boldsymbol{\psi}_t) \|^2] \\
\ell_{\text{Eu}} &= 1 - 2 \times \text{Precison}_{\text{cd}} \times \text{Recall}_{\text{cd}} / (\text{Precison}_{\text{cd}} + \text{Recall}_{\text{cd}})
\end{aligned} \tag{19}$$

where  $\lambda \in [0,1]$  is the weighted coefficient,  $\boldsymbol{\varphi}_{\text{cd}}^\theta$  indicates the parameterized denoiser,  $\boldsymbol{\varphi}_{\text{cd}} \sim \mathcal{N}(0, \mathbf{I})$  indicates random noise from a Gaussian distribution in change detection, and  $\mathbf{Y}_0$  represents the initial change detection result.  $\boldsymbol{\psi}_t$  is a function approximator aimed to predict  $\boldsymbol{\psi}$  from  $\mathbf{Y}_t$ .  $\text{Precison}_{\text{cd}}$  and  $\text{Recall}_{\text{cd}}$  are the precision and recall values to evaluate the truth label and predicted label in the uncertain region.

## 4. Experiment and Result

To verify the superiority of UDHF<sup>2</sup>-Net in semantic segmentation and change detection tasks of RSIHI, comprehensive experiments are conducted to compare with the several advanced networks on public benchmark datasets.

### 4.1 Semantic segmentation task

#### 4.1.1 Datasets

Excellent and remarkable public benchmark datasets for remote sensing semantic segmentation are leveraged to evaluate the proposed network. The datasets are described as follows:

**ISPRS Vaihingen 2D Dataset.** The dataset was collected by the International Society for Photogrammetry and Remote Sensing from Vaihingen, which has four bands (i.e., near-infrared, red, and green bands). It consists of 33 true orthophoto images, one of which has the size of 2494×2064 pixels with ground sampling distance of 9 cm. It is divided into training, validation and testing datasets, including 17, 1 and 15 images respectively. This dataset is cut into the same size patches of 512×512 pixels with a sliding window striding 256 pixels. It consists of six categories, namely, impervious surfaces, buildings, low vegetation, trees, cars, and clutter/background. Notably some occluded buildings by low vegetation or trees could be corrected and recovered.

**ISPRS Potsdam 2D Dataset.** The dataset was collected by the International Society for Photogrammetry and Remote Sensing from a 1.38 km<sup>2</sup> area of Potsdam with four bands (i.e., near-infrared, red, green and blue bands). It consists of 38 true orthophoto images, one of which has the size of 6000×6000 pixels with ground sampling distance of 9 cm. It is divided into training, validation and testing datasets, including 23, 1 and 14 images respectively. This dataset is cut into the same size patches of 512×512 pixels using a sliding window striding 256 pixels. It consists of the same six categories as the ISPRS Vaihingen 2D Dataset. Notably some occluded buildings by low vegetation or trees could be corrected and recovered.

#### 4.1.2 Comparison methods

To confirm the effectiveness of the proposed UDHF<sup>2</sup>-Net, several comparative

DNNs for semantic segmentation task were chosen as the following: MAResU-Net (Li et al., 2022), SwiftNet (Wang et al., 2021a), ABCNet (Li et al., 2021b), Segmenter (Borland et al., 2021), BANet (Wang et al., 2021b), Swin Transformer (Liu et al., 2021), FT-UNetFormer (Wang et al., 2022a), DeepLabV3+ (Chen et al., 2017), PSPNet (Zhao et al., 2017), LANet (Ding et al., 2021), MANet (Li et al., 2021a), HRNetV2 (Wang et al., 2020), HRFormer (Yuan et al., 2021), EaNet (Zheng et al., 2020), SFFNet (Yang et al., 2024).

#### *4.1.3 Implementation details*

All experiments were conducted using the PyTorch framework on four NVIDIA GTX 3090Ti GPU.

**Hyperparameter setting.** The AdamW optimizer was chosen to train all networks in semantic segmentation task. Specially, we conducted the cosine strategy with an initial learning rate of 10-4 to adjust learning rate. The batchsize and epoch were set to 4 and 100 respectively.

**Data augmentation strategy.** Some data augmentation strategies were chosen such as random scaling ([0.5, 0.75, 1.0, 1.25, 1.5]), random vertical and horizontal flipping.

#### *4.1.4 Evaluation metrics*

To evaluate the effectiveness of the proposed UDHF<sup>2</sup>-Net, the following metrics are chosen as the following: overall accuracy (OA), F1 score (F1), mean F1 score and mean intersection over union (mIoU).

### *4.2 Change detection task*

#### *4.2.1 Datasets*

Excellent and remarkable public benchmark datasets are leveraged to evaluate the proposed semi-pseudo-Siamese UDHF<sup>2</sup>-Net for change detection task, which are described as follows:

**WHU building change detection dataset** (WB-CD dataset). The WB-CD dataset was sampled from two cities, i.e., Christchurch and New Zealand in 2012 and 2016. It consists of a pair image with a size of  $15354 \times 32507$  pixels at a spatial resolution of

0.2 m. The image pairs were cut into non-overlapping pair samples with a size of  $256 \times 256$  pixels to generate the training, validation and test datasets in the ratio of 1:1:8.

**LEVIR-CD dataset.** The LEVIR-CD dataset is a collection of building dataset obtained from Google Earth imagery with a high spatial resolution of 0.5m. It includes 31333 pairs of change instances, which were divided into 10192 pairs of image patches with a size of  $256 \times 256$  pixels to generate 7120 pairs of non-overlapping images for training, 1024 pairs of images for validating and 2048 pairs of images for testing.

#### *4.2.2 Comparison methods*

To confirm the effectiveness of the proposed semi-pseudo-Siamese UDHF<sup>2</sup>-Net, several comparative DNNs for change detection task were chosen as following: AMTNet (Liu et al., 2023), FC-EF (Caye Daudt et al., 2018), FC-Siam-conc (Caye Daudt et al., 2018), FC-Sima-diff (Caye Daudt et al., 2018), DTCDSCN (Liu et al., 2020), SNUNet (Fang et al., 2022), BiT (Chen et al., 2022), MTCNet (Wang et al., 2022c), GAS-Net (Zhang et al., 2023a), W-Net (Wang et al., 2023b), ChangerEX (Fang et al., 2023), P2V-CD (Lin et al., 2023), ChangeFormer (Bandara and Patel, 2022), SGSLN (Zhao et al., 2023), IFN (Zhang et al., 2020b), MFPNet (Xu et al., 2021).

#### *4.2.3 Implementation details*

All experiments were conducted using the PyTorch framework on four NVIDIA GTX 3090Ti GPU.

**Hyperparameter setting.** We chose the AdamW function as the optimizer to train all networks in change detection task. And the AdamW optimizer was chosen to train all networks. And the cosine strategy was implemented with an initial learning rate of 10-4. The batchsize were set to 8, and epoch were set to 100.

**Data augmentation strategy.** The following data augmentation strategies were conducted: random scaling in the range from 0.5 to 2.0, random vertical and horizontal flipping.

#### *4.2.4 Evaluation metrics*

To evaluate the effectiveness of the proposed semi-pseudo-Siamese UDHF<sup>2</sup>-Net, the following metrics are chosen as the following: Precision, Recall, F1 score (F1) and

intersection over union (IoU).

### 4.3 Result

#### 4.3.1 Semantic segmentation results

##### (1) Experiments on ISPRS Potsdam dataset

**Table 1**

Quantitative analysis results on the ISPRS Potsdam test dataset with comparison DNNs. The highest values are highlighted in bold for every evaluation metric.

Method	Backbone	F1					MeanF1	OA	mIoU
		Imp.surf.	Building	Lowveg.	Tree	Car			
SwiftNet (Wang et al., 2021)	ResNet18	91.83	95.94	85.72	86.84	94.46	90.96	89.33	83.84
ABCNet (Li et al., 2021b)	ResNet18	93.50	96.90	87.90	89.10	95.80	92.70	91.30	86.50
Segmenter (Borland et al., 2021)	ViT-Tiny	91.50	95.30	85.40	85.00	88.50	89.20	88.70	80.70
BANet (Sun et al., 2021)	ResT-Lite	93.34	96.66	87.37	89.12	95.99	92.50	91.06	86.25
Swin Transformer (Liu et al., 2021)	Swin-Tiny	93.20	96.40	87.60	88.60	95.40	92.20	90.90	85.80
FT-UNetFormer (Wang et al., 2022b)	Swin-Base	93.90	97.20	88.80	<b>89.80</b>	96.60	93.30	92.00	87.50
DeepLabV3+ (Chen et al., 2017)	ResNet18	90.53	95.89	83.61	84.25	88.69	88.59	87.97	80.56
PSPNet (Zhao et al., 2017)	ResNet18	90.56	95.65	84.61	84.72	88.49	90.51	88.28	80.32
LANet (Ding et al., 2021)	ResNet18	93.05	97.19	87.30	88.04	94.19	91.95	90.84	-
MANet (Li et al., 2021a)	ResNet50	93.25	96.63	87.99	88.95	96.39	92.64	91.05	89.01
SFFNet (Yang et al., 2024)	-	93.73	97.02	89.02	90.26	96.79	93.36	91.88	87.73
HRNetV2 + OCR (Wang et al., 2020)	HRNetV2-W48	91.92	96.16	85.65	86.97	94.63	91.07	89.63	83.94
HRFormer-B+OCR+SegFix (Yuan et al., 2021)	HRFormer-B	93.31	96.35	87.74	88.43	95.64	92.29	91.12	85.93
Ours		<b>95.29</b>	<b>98.21</b>	<b>89.05</b>	<b>89.71</b>	<b>98.06</b>	<b>94.18</b>	<b>93.86</b>	<b>89.43</b>

As reported in Table 1, the proposed UDHF<sup>2</sup>-Net yielded the highest mIoU value of 89.43%, the highest OA value of 93.86% and the highest MeanF1 94.18 on the ISPRS Potsdam test dataset, exceeding all advanced comparison networks. It is worth noting that the proposed UDHF<sup>2</sup>-Net not only outperforms HRNet by 5.49% and HRFormer by 3.5% in mIoU, but also exceeds UNetFormer by 1.93%. Especially, for some classes of regular objects that are sensitive to edges such as buildings, impervious surfaces and cars, UDHF<sup>2</sup>-Net achieves the highest values in IoU than all advanced comparison networks. Additionally, the results of segmentation and visualization on the ISPRS Potsdam dataset also illustrates the superiority and effectiveness of the proposed UDHF<sup>2</sup>-Net as shown in Fig.6.

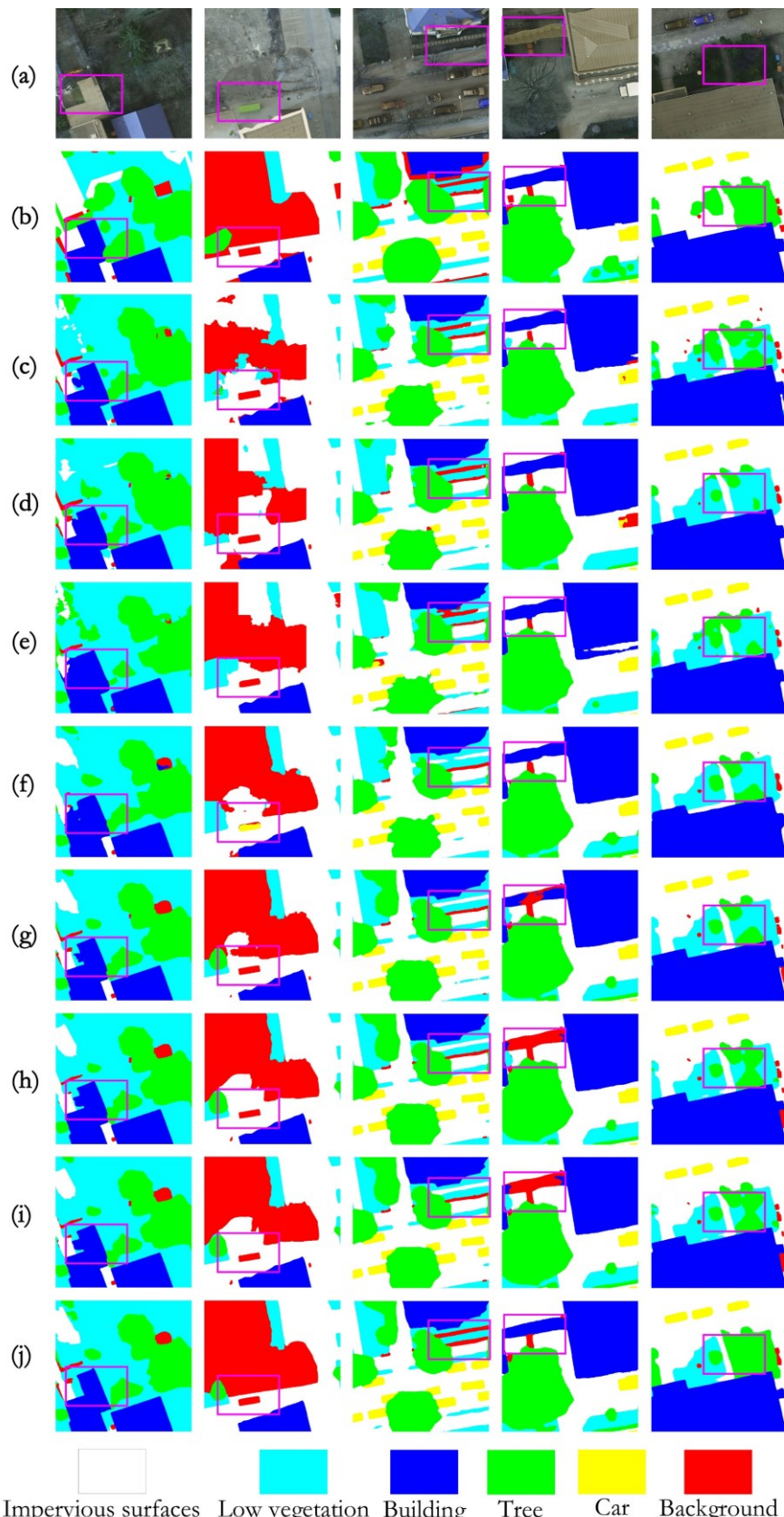


**Figure 6.** The visualization results of the comparative networks on the ISPRS Potsdam test dataset: (a) the RGB image; (b) the true labels; (c) PSPNet; (d) DeeplabV3+; (e) HRNet; (f) SwinUpNet; (g)HRFormer; (h) Segformer; (i) FT-

UNetFormer; (j) UDHF<sup>2</sup>-Net. The purple boxes highlight the edge segmentation details.

### (2) Experiments on ISPRS Vaihingen dataset

**Table 2**

Quantitative analysis results on the ISPRS Vaihingen test dataset for comparison DNNs. The highest values are highlighted in bold for every evaluation metric.

Method	Backbone	F1				MeanF1	OA	mIoU
		Imp.surf.	Building	Lowveg.	Tree			
<b>MAResU-Net</b> (Li et al., 2022b)	ResNet18	92.91	95.26	84.95	89.94	88.33	90.28	90.86
<b>SwiftNet</b> (Wang et al., 2021)	ResNet18	92.22	94.84	84.14	89.31	81.23	88.35	90.20
<b>ABCNet (Li et al., 2021b)</b>	ResNet18	92.70	95.20	84.50	89.70	85.30	89.50	90.70
Segmenter (Borland et al., 2021)	ViT-Tiny	89.80	93.00	81.20	88.90	67.60	84.10	88.10
<b>BANet</b> (Wang et al., 2021b)	ResT-Lite	92.23	95.23	83.75	89.92	86.76	89.58	90.48
Swin Transformer (Liu et al., 2021)	Swin-Tiny	92.80	95.60	85.10	90.60	85.10	89.80	91.00
FT-UNetFormer (Wang et al., 2022b)	Swin-Base	93.50	96.00	85.60	<b>90.80</b>	90.40	91.30	91.60
<b>EaNet (Zheng et al., 2020)</b>	ResNet101	93.40	96.20	85.60	90.50	88.30	90.80	91.20
DeepLabV3+ (Chen et al., 2017)	ResNet18	91.35	94.34	81.32	87.42	78.14	86.60	88.91
PSPNet (Zhao et al., 2017)	ResNet18	91.44	94.38	81.52	87.91	78.02	86.65	88.99
<b>LANet</b> (Ding et al., 2021)	ResNet18	92.41	94.90	82.89	88.92	81.31	88.09	89.83
<b>MANet</b> (Li et al., 2021a)	ResNet50	93.02	95.47	84.64	89.97	88.95	90.41	90.96
SFFNet (Yang et al., 2024)	-	93.51	96.25	85.94	91.43	91.24	91.67	91.91
HRNetV2 + OCR (Wang et al., 2020)	HRNetV2-W48	92.34	94.92	83.89	89.54	82.36	88.61	90.41
HRFormer-B+OCR+SegFix (Yuan et al., 2021)	B	92.91	95.63	84.34	90.56	87.33	90.15	91.24
Ours		<b>94.23</b>	<b>96.92</b>	<b>85.79</b>	90.65	<b>91.39</b>	<b>91.8</b>	<b>93.24</b>
								<b>85.23</b>

As reported in Table 2, the proposed UDHF<sup>2</sup>-Net illustrates the highest mIoU value of 85.23%, the highest OA value of 93.24% and the highest MeanF1 of 91.80% on the ISPRS Vaihingen test dataset. These values outperform those of all advanced comparison networks. Specifically, UDHF<sup>2</sup>-Net even yields the highest F1 values for per-class. Notably, it improves the segmentation representation in the edge regions, such as buildings, impervious surfaces and cars. Concretely, the visual segmentation results on ISPRS Vaihingen test dataset were provided to verify the outstanding performance of our UDHF<sup>2</sup>-Net than other current networks as illustrated in Fig.7.

### (3) Ablation experiments

This section presents detailed ablation experiments to evaluate the rationality and effectiveness of every components of the proposed UDHF<sup>2</sup>-Net on ISPRS Potsdam test

dataset.

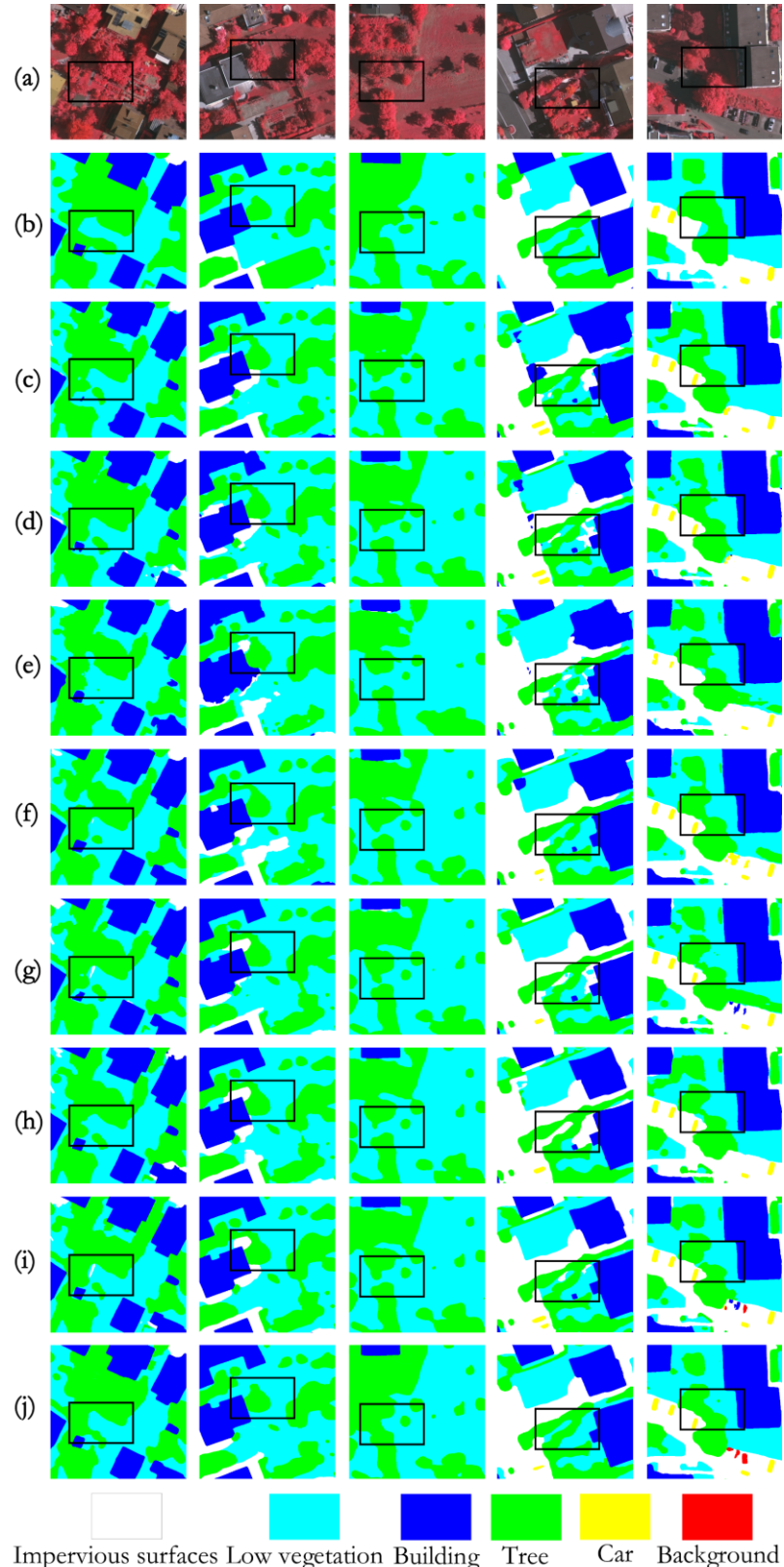


**Figure 7.** The visualization results of the comparative networks on the ISPRS Vaihingen test dataset: (a) the RGB image; (b) the true labels; (c) PSPNet; (d) DeeplabV3+; (e) HRNet; (f) SwinUpNet; (g)HRFormer; (h) Segformer; (i) FT-UNetFormer; (j) UDHF<sup>2</sup>-Net. The black boxes highlight the edge segmentation details.

Table 3 validates the effectiveness of UDHF<sup>2</sup>-Net with combination strategy of different frequency streams on the ISPRS Potsdam test dataset. Two single frequency representation strategies are compared as following: UDHF<sup>2</sup>-Net with retained the spatially stationary frequency streams, and UDHF<sup>2</sup>-Net with retained the spatially non-stationary frequency streams. According to this result, it is observed that the combination of spatially stationary and non-stationary frequency streams outperforms the single frequency streams for all evaluation metrics.

Table 4 reports the effectiveness of the proposed MUDM on the ISPRS Potsdam test dataset. With the assistance of MUDM, the initial segmentation result is further optimized to improve the MeanF1 value by 0.32%, the OA value by 0.41%, the mIoU by 0.52% compared with UDHF<sup>2</sup>-Net without MUDM. Fig.8 demonstrates the visualization results of MUDM. In Fig.8(c), MUDM demonstrates the outstanding performing for recovering the occluded building completely.

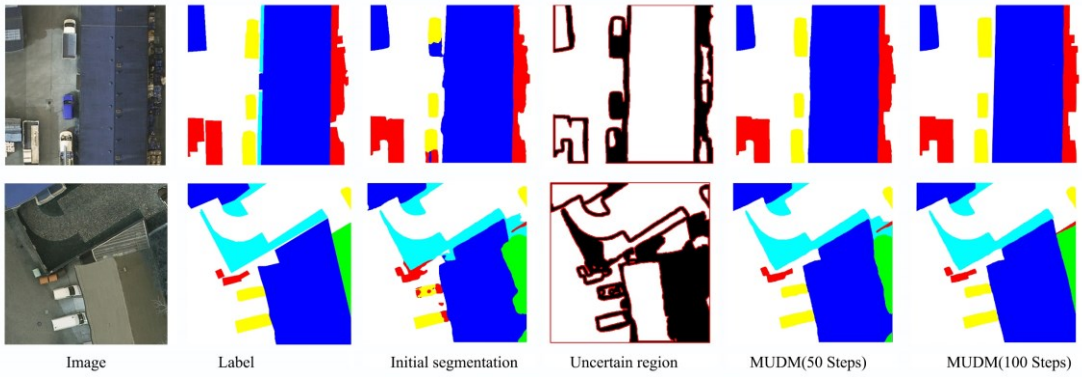


**Figure 8.** The visualization results of MUDM.

Table 5 indicates the significant performance of the proposed spatially stationary-and-non-stationary multi-frequency fusion decoder. Compared to other some outstanding decoders, our proposed decoder achieves the improvement gains at least 0.39% in MeanF1, 0.62% in OA and 0.67% in mIoU. According to this result, this proposed decoder could effectively combine spatially stationary and non-stationary frequency features to restore to the original resolution for achieving segmentation results compared with the current decoders.

Table 6 indicates that the superiority of the proposed HFTM. HFTM outperforms the HRFormer module with performance gains of 0.5% mIoU, 0.22% MeanF1 and 0.24%

OA respectively. Compared with HRFormer module, these results indicate that HFTM has a more powerful capability of frequency feature representation, which benefits from the larger receptive fields of deformable convolution.

**Table 3**

Performance for UDHF<sup>2</sup>-Net with combination strategy of different frequency streams on ISPRS test Potsdam. The highest values are highlighted in bold for every evaluation metric.

Method	Spatially stationary frequency streams	Spatially non-stationary frequency streams	MeanF1	OA	mIoU
UDHF <sup>2</sup> -Net	✓	✗	93.08	92.97	88.32
UDHF <sup>2</sup> -Net	✗	✓	93.21	93.01	88.46
UDHF <sup>2</sup> -Net	✓	✓	<b>94.18</b>	<b>93.86</b>	<b>89.43</b>

**Table 4**

Performance for the mask-and-geo-knowledge-based uncertainty diffusion module (MUDM) on ISPRS test Potsdam. The highest values are highlighted in bold for every evaluation metric.

Method	SHCP	MUDM	MeanF1	OA	mIoU
UDHF <sup>2</sup> -Net	✓	✗	93.86	93.45	88.91
UDHF <sup>2</sup> -Net	✓	✓	<b>94.18</b>	<b>93.86</b>	<b>89.43</b>

**Table 5**

Performance for the spatially stationary-and-non-stationary multi-frequency fusion decoder on ISPRS test Potsdam. The highest values are highlighted in bold for every evaluation metric.

Method	Encoder	Decoder	MeanF1	OA	mIoU
UDHF <sup>2</sup> -Net	SSHT	UPerNet	93.72	93.18	88.68
UDHF <sup>2</sup> -Net	SSHT	OCR	93.79	93.24	88.76
UDHF <sup>2</sup> -Net	SSHT	Spatially stationary-and-non-stationary multi-frequency fusion decoder	<b>94.18</b>	<b>93.86</b>	<b>89.43</b>

**Table 6**

Performance for High-frequency Transformer module on ISPRS test Potsdam. The highest values are highlighted in bold for every evaluation metric.

Method	High-frequency Transformer module	HRFormer module	MeanF1	OA	mIoU
UDHF <sup>2</sup> -Net	✗	✓	93.96	93.62	88.93
UDHF <sup>2</sup> -Net	✓	✗	<b>94.18</b>	<b>93.86</b>	<b>89.43</b>

### 4.3.2 Change detection results

#### (1) Experiments on WHU building dataset

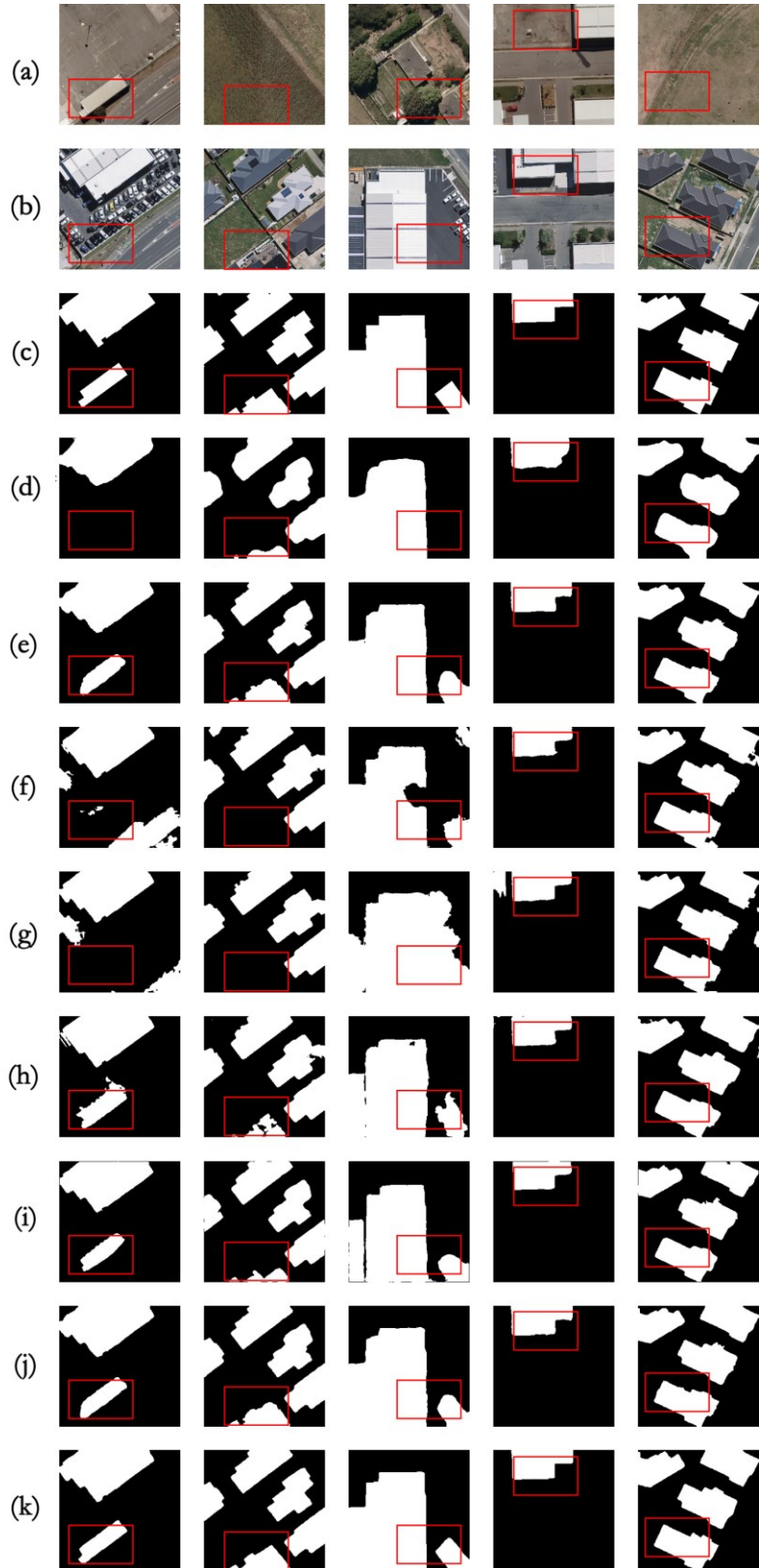


**Figure 9.** The visualization results of the different networks on the WHU building dataset: (a) the RGB image of the first date; (b) the RGB image of the second date; (c) the true labels; (d) FC-Siam-conc; (e) FC-Siam-diff; (f) SNUNet; (g) BiT; (h) IFNet; (i) P2V-CD; (j) ChangeFormer; (k) semi-pseudo-Siamese UDHF<sup>2</sup>-Net. The red boxes highlight the edge extraction details.

**Table 7**

Quantitative analysis results on the WHU building test dataset for different DNNs. The highest values are highlighted in bold for every evaluation metric.

Method	Precision	Recall	F1 score	IoU
AMTNet (Liu et al., 2023)	92.86	91.99	92.42	85.64
FC-EF (Caye Daudt et al., 2018)	80.87	75.43	78.05	64.01
FC-Siam-conc (Caye Daudt et al., 2018)	68.62	87.30	76.84	62.39
FC-Sima-diff (Caye Daudt et al., 2018)	70.45	77.62	73.86	58.56
DSIFN/IFN (Zhang et al., 2020b)	91.47	81.57	86.24	75.99
DTCDSNC (Liu et al., 2020)	-	89.32	89.01	79.08
SNUNet (Fang et al., 2022)	83.25	91.35	87.11	77.17
BiT (Chen et al., 2022)	86.64	81.48	83.98	72.39
ChangeFormer (Bandara and Patel, 2022)	92.89	85.60	88.82	79.89
MTCNet (Wang et al., 2022c)	-	91.90	82.65	70.43
SGSLN/512 (Zhao et al., 2023)	96.11	93.64	94.86	90.22
W-Net (Wang et al., 2023b)	94.76	88.88	91.72	-
P2V-CD (Lin et al., 2023)	95.48	89.47	92.38	-
Ours	<b>97.03</b>	<b>93.85</b>	<b>95.41</b>	<b>90.64</b>

As observed in Table 7, the proposed semi-pseudo-Siamese UDHF<sup>2</sup>-Net obtains the best performance representation than other compared networks in all evaluation metrics, achieving up to 97.03% in Precision, 93.85% in Recall, 95.41% in F1, 90.64% in IoU on the WHU building test dataset. It validated that the extended semi-pseudo-Siamese UDHF<sup>2</sup>-Net also obtains the efficient performance in the change detection task. Concretely, the visual representation is provided to verify illustrates the robustness of the edge segmentation details, which outperforms the compared optimal network as shown in Fig.9.

## (2) Experiments on LEVIR-CD dataset

**Table 8**

Quantitative analysis results on the LEVIR-CD test dataset for different DNNs. The highest values are highlighted in bold for every evaluation metric.

Method	Precision	Recall	F1 score	IoU
AMTNet (Liu et al., 2023)	91.82	89.71	90.76	83.08
FC-EF (Caye Daudt et al., 2018)	86.91	80.17	83.4	71.53
FC-Siam-conc (Caye Daudt et al., 2018)	91.99	76.77	83.69	71.96
FC-Sima-diff (Caye Daudt et al., 2018)	89.53	83.31	86.31	75.92
DSIFN/IFN (Zhang et al., 2020b)	88.53	86.83	87.67	78.05
SNUNet (Fang et al., 2022)	89.18	87.17	88.16	78.83
BiT (Chen et al., 2022)	89.24	89.37	89.31	80.68
ChangeFormer (Bandara and Patel, 2022)	92.05	88.80	90.40	82.48

MTCNet (Wang et al., 2022c)	-	89.62	90.24	82.22
GAS-Net (Zhang et al., 2023a)	91.82	90.62	91.21	-
W-Net (Wang et al., 2023b)	91.24	89.21	90.31	-
SGSLN/512 (Zhao et al., 2023)	93.07	<b>91.61</b>	92.33	85.76
P2V-CD (Lin et al., 2023)	93.32	90.60	91.94	-
ChangerEX (Fang et al., 2023)	93.61	90.56	92.06	-
<b>Ours</b>	<b>93.82</b>	91.22	<b>92.5</b>	<b>85.79</b>

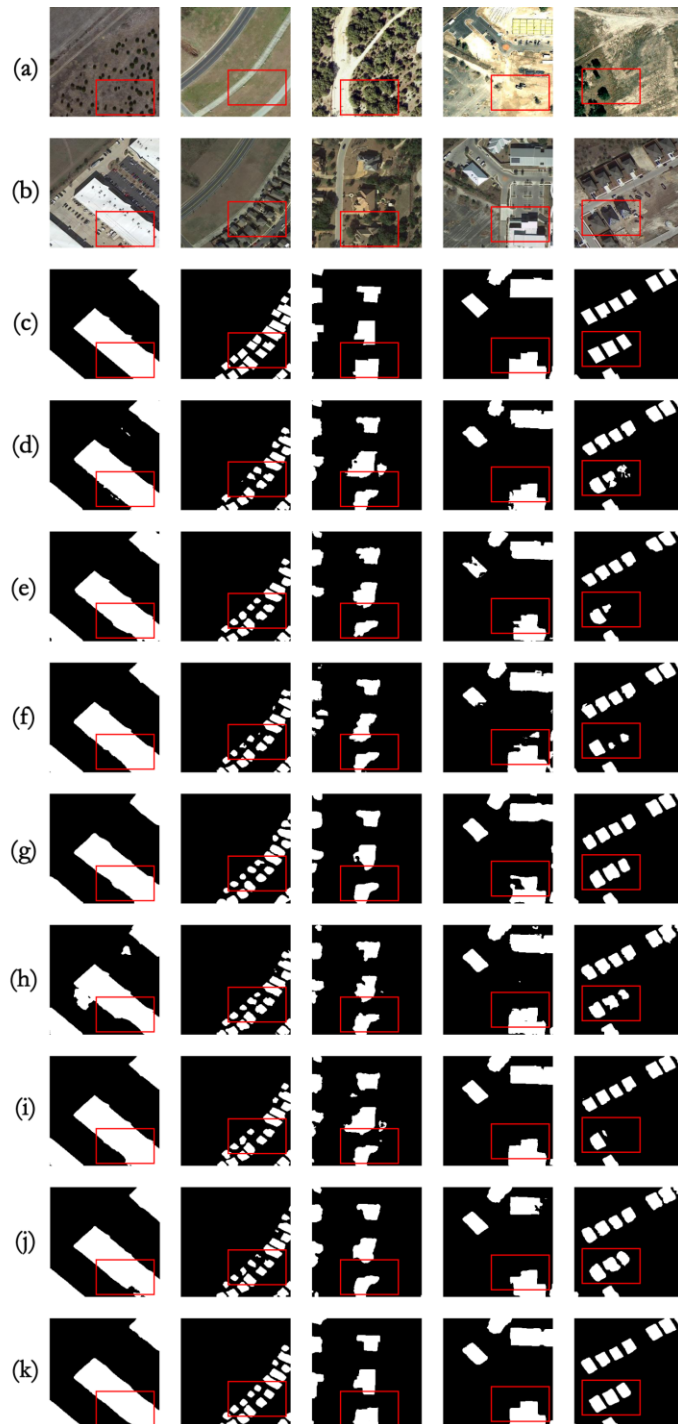


**Figure 10.** The visualization results of the different networks on the LEVIR-CD dataset: (a) the RGB image of the first date; (b) the RGB image of the second date; (c)

the true labels; (d) FC-Siam-conc; (e) FC-Siam-diff; (f) SNUNet; (g) BiT; (h) IFNet; (i) P2V-CD; (j) ChangeFormer; (k) semi-pseudo-Siamese UDHF<sup>2</sup>-Net. The red boxes highlight the edge extraction details.

As observed in Table 8, the proposed semi-pseudo-Siamese UDHF<sup>2</sup>-Net obtain the best performance representation in all evaluation metrics (up to 93.82% in Precision, 91.22% in Recall, 92.5% in F1, 85.79% in IoU) than other compared networks on the LEVIR-CD test dataset. It verified the extendedly semi-pseudo-Siamese UDHF<sup>2</sup>-Net also obtains the efficient performance in the change detection task. Concretely, the detailed change results and visual representation are provided to verify illustrates the robust representation in edge segmentation details which outperforms the compared optimal network in IoU as shown in Fig.10.

### (3) Ablation experiments

Detailed ablation experiments are conducted to evaluate the rationality and effectiveness of every components of the proposed semi-pseudo-Siamese UDHF<sup>2</sup>-Net on LEVIR-CD test dataset.

**Table 9**

Performance for semi-Pseudo-Siamese UDHF<sup>2</sup>-Net with different frequency streams on LEVIR-CD test dataset. The highest values are highlighted in bold for every evaluation metric.

Method	Spatially stationary frequency streams	Spatially-non-stationary frequency streams	Precision	Recall	F1	IoU
Semi-Pseudo-Siamese UDHF <sup>2</sup> -Net	√	✗	93.27	90.84	92.04	85.40
Semi-Pseudo-Siamese UDHF <sup>2</sup> -Net	✗	√	93.12	91.09	92.09	85.53
Semi-Pseudo-Siamese UDHF <sup>2</sup> -Net	√	√	<b>93.82</b>	<b>91.22</b>	<b>92.5</b>	<b>85.79</b>

**Table 10**

Performance for the mask-and-geo-knowledge-based uncertainty diffusion module (MUDM) on LEVIR-CD test dataset. The highest values are highlighted in bold for every evaluation metric.

Method	SHCP-based semi-pseudo-Siamese architecture	MUDM	Precision	Recall	F1	IoU
Semi-Pseudo-Siamese UDHF <sup>2</sup> -Net	√	✗	93.01	90.84	91.91	85.24

Semi-Pseudo-Siamese UDHF <sup>2</sup> -Net	√	√	<b>93.82</b>	<b>91.22</b>	<b>92.5</b>	<b>85.79</b>
---	---	---	--------------	--------------	-------------	--------------

**Table 11**

Performance for semi-pseudo-Siamese UDHF<sup>2</sup>-Net on LEVIR-CD test dataset comparing with the difference-based architecture. The highest values are highlighted in bold for every evaluation metric.

Method	Precision	Recall	F1	IoU
SHCP-based differencing architecture	92.25	89.47	90.82	83.54
Semi-Pseudo-Siamese UDHF <sup>2</sup> -Net	<b>93.82</b>	<b>91.22</b>	<b>92.5</b>	<b>85.79</b>

**Table 12**

Performance for High-frequency Transformer module (HFTM) on LEVIR-CD test dataset. The highest values are highlighted in bold for every evaluation metric.

Method	HFTM	HRFormer module	Precision	Recall	F1	IoU
Semi-Pseudo-Siamese UDHF <sup>2</sup> -Net	×	√	93.15	91.00	92.06	85.42
Semi-Pseudo-Siamese UDHF <sup>2</sup> -Net	√	×	<b>93.82</b>	<b>91.22</b>	<b>92.5</b>	<b>85.79</b>

Table 9 reports the superiority of the Semi-Pseudo-Siamese UDHF<sup>2</sup>-Net on LEVIR-CD dataset. Two compared strategies, i.e., Semi-Pseudo-Siamese UDHF<sup>2</sup>-Net with retained spatially non-stationary frequency streams and retained spatially-stationary frequency streams, are implemented to demonstrate the better performance gains by 0.26% of IoU, 0.41% of F1, 0.55% of Precision and 0.13% of Recall respectively than the best two compared modules. That indicates that the complementarity of multiple stationary and non-stationary feature streams can effectively improve accuracy.

Table 10 reports the effectiveness of the proposed MUDM on LEVIR-CD dataset. The results demonstrate that MUDM is also advantageous for the remote sensing change detection task, outperforming the network without MUDM by 0.59% IoU, 0.55% F1, 0.81% Precision and 0.38% Recall respectively. And the visualization results of MUDM are shown in Fig.11.

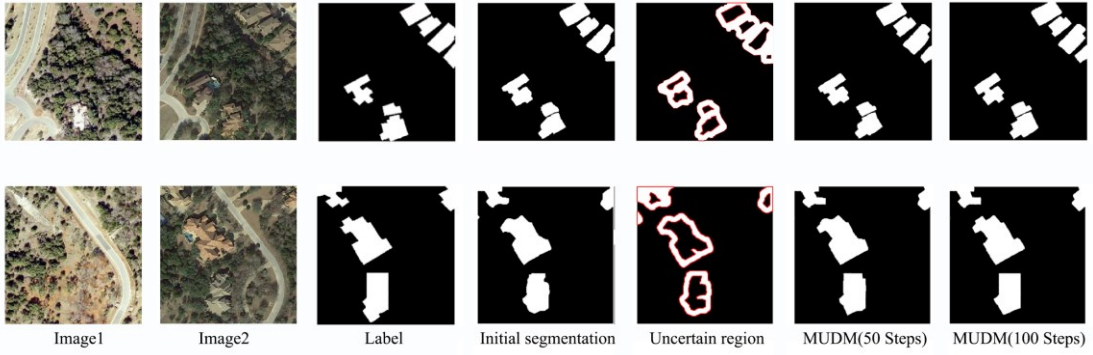


**Figure 11.** The visualization results of MUDM in change detection.

Table 11 reports the effectiveness of semi-pseudo-Siamese UDHF<sup>2</sup>-Net on LEVIR-CD dataset for the remote sensing change detection task. The difference-based architecture replaces the SHCN-based semi-pseudo-Siamese architecture to form change intensity information. Compared with the difference-based architecture, the semi-pseudo-Siamese UDHF<sup>2</sup>-Net obtains the better improvement by 2.25% of IoU, 1.68% of F1, 1.57% of Precision and 1.75% of Recall respectively.

Table 12 reports the effectiveness of the proposed HFTM on LEVIR-CD dataset for the remote sensing change detection task. HFTM achieves the better improvement of change segmentation by 0.37% of IoU, 0.44% of F1, 0.67% of Precision and 0.22% of Recall respectively over the HRFormer module.

## 5. Discussion

### 5.1 Addressing frequency complementarity problem

The proposed SHCP could effectively address the frequency complementarity issue and yield outstanding edge segmentation accuracy. As demonstrated in Table 3 and 9, the ablation experiment results showcase the superiority of this integrated frequency representation scheme over a single non-stationary and stationary frequency representation scheme whether in semantic segmentation or change detection tasks. The rationality of this method is attributed to the intrinsic mechanisms that it has attempted and resolved the complementarity between spatial stationarity and non-stationarity frequency features. It is similar to combining the ability of global feature representation and local feature representation, which has been validated as an effective approach (Jia and Yao, 2023; Zhang et al., 2023b). Different from the current researches, we further have explored to enhance their respective strengths of capturing global consistent

information for spatially stationary frequency features and local abrupt change information for spatially non-stationary frequency features from a frequency domain perspective.

### *5.2 Addressing edge uncertainty problem*

The proposed UDHF<sup>2</sup>-Net demonstrates the superiority to address the edge uncertainty problem. As shown in Table 1, 2, 7 and 8, UDHF<sup>2</sup>-Net achieved excellent performance than the other compared networks. The scientificity of UDHF<sup>2</sup>-Net benefits from the following aspects:

(1) High frequency information is conducive to improving the edge extraction accuracy. Importantly, high frequency features are sensitive for edge details (Shan et al., 2021). The proposed SHCP could deliver high-frequency feature stream in the whole encoder-decoder process to remain high-fidelity edge information and reduce the impact of downsampling. And HD-Net (Li et al., 2024) also have verified that the architecture similar to HRFormer is help to achieve lossless edge performance. In addition, each other's respective advantages of spatially stationary and non- stationary high-frequency features can be complemented, which enhances the representation ability of edge details.

(2) Edge loss function is conducive to optimizing the uncertain edge region. To tackle the issue of edge detail degradation, numerous approaches have placed special emphasis on edge loss function to improves edge discrimination (Zheng et al., 2020). Furthermore, we proposed the edge loss function to optimize the network with the constraint of prior probability, which is trade-off way to improve the speed of network fitting and edge extraction accuracy.

(3) Uncertainty diffusion model is conducive to recovering the multiple geo-knowledge-based uncertainties. As shown in Table 4 and Table 10, the experiment results illustrate that the proposed MUDM could further optimize the initial results effectively. That indicates that the proposed MUDM could gradually denoising the multiple geo-knowledge uncertainties to the data distribution of the refined label. Current researches about denoising diffusion probabilistic model has achieved

excellent performance in repairing occlusion issue such as removing cloud (Zou et al., 2024). In addition, this work could better distinguish mixed pixels, recover the buildings/roads occluded by vegetation and reduce the visual interpretation errors.

### *5.3 Addressing false detection problem in change detection*

This proposed semi-pseudo-Siamese UDHF<sup>2</sup>-Net could adaptively address false detection by registration error in change detection task. Simulated registration errors introduced in the change detection task is conducive to improving the edge extraction outcome of the changed region. As shown in Table 7 and Table 8, the proposed network achieves the best F1 and IoU values in WHU building and LEVIR-CD test datasets compared with the current SOTA networks. The core content of semantic segmentation and change detection is similar. The former is a multi-classification problem, while the latter is a binary classification problem. Thus, the aforementioned two methods in section 5.1 and 5.2 are also effective to enhance edge detail performance in change detection task. Different from semantic segmentation, change detection is easily affected by registration errors, which generally could result in false detection. To overcome this issue, the proposed semi-pseudo-Siamese UDHF<sup>2</sup>-Net adopts MUDM to gradually optimize the edge uncertain region with added registration error noise, which could further enhance the ability of noise resistance. The superiority of this method is reflected in the following aspects:

Firstly, the miss detection could be effectively reduced. For example, several buildings occluded by vegetation could be completed by the proposed MUDM, which commonly could not be overlooked by current networks. This means that our proposed network is friendly to artificial scenes, which could achieve high-accuracy building edge information to serve for creating and updating the navigation map.

Secondly, the false detection could be effectively reduced. For example, the location transformation of building due to registration errors could produce the false changed regions. Then the proposed network could adaptively align multi-frequency features of bi-temporal image to correct registration errors, and further repair unregistered regions in edge.

In addition, mixed pixels generally lead to false and miss detection. To tackle noise is added to train the proposed network for enhancing the robustness of edge extraction. And the proposed network adopts MUDM to improve geometric consistency, the continuity and regularity of edges.

## 6. Conclusion

To performance high-accuracy planetary observation, UDHF<sup>2</sup>-Net is the first to be proposed to realize RSIHI including semantic segmentation and change detection tasks. This UDHF<sup>2</sup>-Net has the following superiority: (1) a spatially-stationary-and-non-stationary high-frequency connection paradigm (SHCP) is proposed to have complementary advantages between spatially stationary and non-stationary frequency features, and deliver high-fidelity edge details through the whole encoder-decoder process for improving the edge extraction accuracy; (2) a mask-and-geo-knowledge-based uncertainty diffusion module (MUDM) is proposed to reduce the edge extraction uncertainty and improve the edge noise resistance; (3) a semi-pseudo-Siamese UDHF<sup>2</sup>-Net is proposed to adaptively reduce the registration errors and improve the edge extraction accuracy of change regions for change detection task. Extensive experiments indicate the effectiveness of the proposed UDHF<sup>2</sup>-Net over different remote sensing image interpretation tasks. In the future, we will further enhance the deep fusion of spatially stationary and non-stationary frequency features to improve computational efficiency. Meanwhile, we hope that the proposed work could encourages more scholars dedicated to deeply explore the potential and possibility of frequency-based visual expression.

## Acknowledgements

The authors are grateful for the comments and contributions of the editors, anonymous reviewers and the members of the editorial team. This work was supported by the Key Program of the National Natural Science Foundation of China under Grant Nos. 42030102, National Natural Science Foundation of China (NSFC) under Grant Nos. 41771493 and 41101407, and the Fundamental Research Funds for the Central Universities under Grant CCNU22QN019.

### **Declaration of competing interest**

The authors declare that they have no known competing financial interests or personal relationships that could have appeared to influence the work reported in this paper.

## Reference:

Bai, J., Ren, J., Yang, Y., Xiao, Z., Yu, W., Havyarimana, V., Jiao, L., 2021. Object detection in large-scale remote-sensing images based on time-frequency analysis and feature optimization. *IEEE Transactions on Geoscience and Remote Sensing* 60, 1-16.

Bai, T., Wang, L., Yin, D., Sun, K., Chen, Y., Li, W., Li, D., 2022. Deep learning for change detection in remote sensing: a review. *Geo-spatial Information Science* 0, 1-27.

Ball, J.E., Wei, P., 2018. Deep Learning Hyperspectral Image Classification using Multiple Class-Based Denoising Autoencoders, Mixed Pixel Training Augmentation, and Morphological Operations, *IGARSS 2018 - 2018 IEEE International Geoscience and Remote Sensing Symposium*6903-6906.

Bandara, W.G.C., Patel, V.M., 2022. A Transformer-Based Siamese Network for Change Detection, *IGARSS 2022 - 2022 IEEE International Geoscience and Remote Sensing Symposium*207-210.

Borland, D., McCormick, C.M., Patel, N.K., Krupa, O., Mory, J.T., Beltran, A.A., Farah, T.M., Escobar-Tomlienovich, C.F., Olson, S.S., Kim, M., 2021. Segmentor: a tool for manual refinement of 3D microscopy annotations. *BMC bioinformatics* 22, 260.

Cao, H., Wang, Y., Chen, J., Jiang, D., Zhang, X., Tian, Q., Wang, M., 2022a. Swin-unet: Unet-like pure transformer for medical image segmentation. *Springer*205-218.

Cao, Y., Huang, X., 2023. A full-level fused cross-task transfer learning method for building change detection using noise-robust pretrained networks on crowdsourced labels. *Remote Sensing of Environment* 284, 113371.

Cao, Y., Wu, Y., Li, M., Liang, W., Hu, X., 2022b. DFAF-Net: A Dual-Frequency PolSAR Image Classification Network Based on Frequency-Aware Attention and Adaptive Feature Fusion. *IEEE Transactions on Geoscience and Remote Sensing* 60, 1-18.

Caye Daudt, R., Le Saux, B., Boulch, A., 2018. Fully Convolutional Siamese Networks for Change Detection, *2018 25th IEEE International Conference on Image Processing (ICIP)*4063-4067.

Chaudhary, S., Taran, S., Bajaj, V., Sengur, A., 2019. Convolutional Neural Network Based Approach Towards Motor Imagery Tasks EEG Signals Classification. *IEEE Sensors Journal* 19, 4494-4500.

Chen, H., Qi, Z., Shi, Z., 2022. Remote Sensing Image Change Detection With Transformers. *IEEE Transactions on Geoscience and Remote Sensing* 60, 1-14.

Chen, L.-C., Papandreou, G., Kokkinos, I., Murphy, K., Yuille, A.L., 2017. Deeplab: Semantic image segmentation with deep convolutional nets, atrous convolution, and fully connected crfs. *IEEE transactions on pattern analysis and machine intelligence* 40, 834-848.

Chen, L.-C., Zhu, Y., Papandreou, G., Schroff, F., Adam, H., 2018. Encoder-decoder with atrous separable convolution for semantic image segmentation. *Proceedings of the European conference on computer vision (ECCV)*801-818.

Croitoru, F.-A., Hondru, V., Ionescu, R.T., Shah, M., 2023. Diffusion models in vision: A survey. *IEEE Transactions on Pattern Analysis and Machine Intelligence*.

Daudt, R.C., Le Saux, B., Boulch, A., Gousseau, Y., 2019. Multitask learning for large-scale semantic change detection. *Computer Vision and Image Understanding* 187, 102783.

Ding, L., Tang, H., Bruzzone, L., 2021. LANet: Local Attention Embedding to Improve the Semantic Segmentation of Remote Sensing Images. *IEEE Transactions on Geoscience and Remote Sensing* 59, 426-435.

Fang, S., Li, K., Li, Z., 2023. Changer: Feature interaction is what you need for change detection. *IEEE Transactions on Geoscience and Remote Sensing*.

Fang, S., Li, K., Shao, J., Li, Z., 2022. SNUNet-CD: A Densely Connected Siamese Network for Change Detection of VHR Images. *IEEE Geoscience and Remote Sensing Letters* 19, 1-5.

Gao, J., O'Neill, B.C., 2020. Mapping global urban land for the 21st century with data-driven simulations and Shared Socioeconomic Pathways. *Nature communications* 11, 2302.

Guo, Y., He, W., Xia, Y., Zhang, H., 2023. Blind single-image-based thin cloud removal using a cloud perception integrated fast Fourier convolutional network. *ISPRS Journal of Photogrammetry and Remote Sensing* 206, 63-86.

Hantson, S., Andela, N., Goulden, M.L., Randerson, J.T., 2022. Human-ignited fires result in more extreme fire behavior and ecosystem impacts. *Nature communications* 13, 2717.

Haut, J.M., Paoletti, M.E., Plaza, J., Plaza, A., Li, J., 2019. Hyperspectral Image Classification Using Random Occlusion Data Augmentation. *IEEE Geoscience and Remote Sensing Letters* 16, 1751-1755.

He, D., Zhong, Y., Wang, X., Zhang, L., 2021. Deep Convolutional Neural Network Framework for Subpixel Mapping. *IEEE Transactions on Geoscience and Remote Sensing* 59, 9518-9539.

Ho, J., Jain, A., Abbeel, P., 2020. Denoising diffusion probabilistic models. *Advances in neural information processing systems* 33, 6840-6851.

Hong, D., Gao, L., Yao, J., Yokoya, N., Chanussot, J., Heiden, U., Zhang, B., 2021. Endmember-guided unmixing network (EGU-Net): A general deep learning framework for self-supervised hyperspectral unmixing. *IEEE Transactions on Neural Networks and Learning Systems* 33, 6518-6531.

Jia, S., Yao, W., 2023. Joint learning of frequency and spatial domains for dense image prediction. *ISPRS Journal of Photogrammetry and Remote Sensing* 195, 14-28.

Krishnamurthy R, P.K., Fisher, J.B., Choularton, R.J., Kareiva, P.M., 2022. Anticipating drought-related food security changes. *Nature Sustainability* 5, 956-964.

Li, J., Huang, X., Gong, J., 2019. Deep neural network for remote-sensing image interpretation: Status and perspectives. *National Science Review* 6, 1082-1086.

Li, J., Zha, S., Chen, C., Ding, M., Zhang, T., Yu, H., 2022a. Attention guided global enhancement and local refinement network for semantic segmentation. *IEEE Transactions on Image Processing* 31, 3211-3223.

Li, R., Zheng, S., Duan, C., Su, J., Zhang, C., 2022b. Multistage Attention ResU-Net

for Semantic Segmentation of Fine-Resolution Remote Sensing Images. *IEEE Geoscience and Remote Sensing Letters* 19, 1-5.

Li, R., Zheng, S., Zhang, C., Duan, C., Su, J., Wang, L., Atkinson, P.M., 2021a. Multiattention Network for Semantic Segmentation of Fine-Resolution Remote Sensing Images. *IEEE Transactions on Geoscience and Remote Sensing*, 1-13.

Li, R., Zheng, S., Zhang, C., Duan, C., Wang, L., Atkinson, P.M., 2021b. ABCNet: Attentive bilateral contextual network for efficient semantic segmentation of Fine-Resolution remotely sensed imagery. *ISPRS Journal of Photogrammetry and Remote Sensing* 181, 84-98.

Li, X.-Y., Li, X., Fan, Z., Mi, L., Kandakji, T., Song, Z., Li, D., Song, X.-P., 2022c. Civil war hinders crop production and threatens food security in Syria. *Nat Food* 3, 38-46.

Li, X., Diao, W., Mao, Y., Gao, P., Mao, X., Li, X., Sun, X., 2023. OGMN: Occlusion-guided multi-task network for object detection in UAV images. *ISPRS Journal of Photogrammetry and Remote Sensing* 199, 242-257.

Li, Y., Hong, D., Li, C., Yao, J., Chanussot, J., 2024. HD-Net: High-resolution decoupled network for building footprint extraction via deeply supervised body and boundary decomposition. *ISPRS Journal of Photogrammetry and Remote Sensing* 209, 51-65.

Lin, M., Yang, G., Zhang, H., 2023. Transition Is a Process: Pair-to-Video Change Detection Networks for Very High Resolution Remote Sensing Images. *IEEE Trans. on Image Process.* 32, 57-71.

Liu, W., Lin, Y., Liu, W., Yu, Y., Li, J., 2023. An attention-based multiscale transformer network for remote sensing image change detection. *ISPRS Journal of Photogrammetry and Remote Sensing* 202, 599-609.

Liu, Y., Pang, C., Zhan, Z., Zhang, X., Yang, X., 2020. Building change detection for remote sensing images using a dual-task constrained deep siamese convolutional network model. *IEEE Geoscience and Remote Sensing Letters* 18, 811-815.

Liu, Z., Lin, Y., Cao, Y., Hu, H., Wei, Y., Zhang, Z., Lin, S., Guo, B., 2021. Swin Transformer: Hierarchical Vision Transformer Using Shifted Windows, *Proceedings of the IEEE/CVF International Conference on Computer Vision* 10012-10022.

Long, J., Shelhamer, E., Darrell, T., 2015. Fully convolutional networks for semantic segmentation, *Proceedings of the IEEE conference on computer vision and pattern recognition* 3431-3440.

Lyu, Y., Vosselman, G., Xia, G.-S., Yilmaz, A., Yang, M.Y., 2020. UAVid: A semantic segmentation dataset for UAV imagery. *ISPRS Journal of Photogrammetry and Remote Sensing* 165, 108-119.

Papadomanolaki, M., Verma, S., Vakalopoulou, M., Gupta, S., Karantzalos, K., 2019. Detecting urban changes with recurrent neural networks from multitemporal Sentinel-2 data, *IGARSS 2019-2019 IEEE international geoscience and remote sensing symposium*. IEEE214-217.

Pascolini-Campbell, M., Reager, J.T., Chandanpurkar, H.A., Rodell, M., 2021.

RETRACTED ARTICLE: A 10 per cent increase in global land evapotranspiration from 2003 to 2019. *Nature* 593, 543-547.

Peng, D., Zhang, Y., Guan, H., 2019. End-to-end change detection for high resolution satellite images using improved UNet++. *Remote Sensing* 11, 1382.

Qi, X., Zhu, P., Wang, Y., Zhang, L., Peng, J., Wu, M., Chen, J., Zhao, X., Zang, N., Mathiopoulos, P.T., 2020. MLRSNet: A multi-label high spatial resolution remote sensing dataset for semantic scene understanding. *ISPRS Journal of Photogrammetry and Remote Sensing* 169, 337-350.

Qiu, S., Wen, G., Fan, Y., 2017. Occluded Object Detection in High-Resolution Remote Sensing Images Using Partial Configuration Object Model. *IEEE Journal of Selected Topics in Applied Earth Observations and Remote Sensing* 10, 1909-1925.

Ronneberger, O., Fischer, P., Brox, T., 2015. U-Net: Convolutional Networks for Biomedical Image Segmentation, in: Navab, N., Hornegger, J., Wells, W.M., Frangi, A.F. (Eds.). Springer International Publishing 234-241.

Selinger, P., 2017. Potrace: a polygon-based tracing algorithm (2003). URL: <http://potrace>. sourceforge. net 5.

Shan, L., Li, X., Wang, W., 2021. Decouple the High-Frequency and Low-Frequency Information of Images for Semantic Segmentation, *ICASSP 2021 - 2021 IEEE International Conference on Acoustics, Speech and Signal Processing (ICASSP)* 1805-1809.

Shen, H., Lin, L., Li, J., Yuan, Q., Zhao, L., 2020. A residual convolutional neural network for polarimetric SAR image super-resolution. *ISPRS Journal of Photogrammetry and Remote Sensing* 161, 90-108.

Shi, W., Zhang, M., Zhang, R., Chen, S., Zhan, Z., 2020. Change Detection Based on Artificial Intelligence: State-of-the-Art and Challenges. *Remote Sensing* 12, 1688.

Smith, A., Bates, P.D., Wing, O., Sampson, C., Quinn, N., Neal, J., 2019. New estimates of flood exposure in developing countries using high-resolution population data. *Nature communications* 10, 1814.

Strudel, R., Garcia, R., Laptev, I., Schmid, C., 2021. Segmenter: Transformer for semantic segmentation, 7262-7272.

Sun, X., Wang, B., Wang, Z., Li, H., Li, H., Fu, K., 2021. Research Progress on Few-Shot Learning for Remote Sensing Image Interpretation. *IEEE Journal of Selected Topics in Applied Earth Observations and Remote Sensing* 14, 2387-2402.

Sun, X., Wang, P., Yan, Z., Xu, F., Wang, R., Diao, W., Chen, J., Li, J., Feng, Y., Xu, T., Weinmann, M., Hinz, S., Wang, C., Fu, K., 2022. FAIR1M: A benchmark dataset for fine-grained object recognition in high-resolution remote sensing imagery. *ISPRS Journal of Photogrammetry and Remote Sensing* 184, 116-130.

Tanaka, T., Sun, L., Becker-Reshef, I., Song, X.-P., Puricelli, E., 2023. Satellite forecasting of crop harvest can trigger a cross-hemispheric production response and improve global food security. *Commun Earth Environ* 4, 1-9.

Tian, S., Zhong, Y., Zheng, Z., Ma, A., Tan, X., Zhang, L., 2022. Large-scale deep

learning based binary and semantic change detection in ultra high resolution remote sensing imagery: From benchmark datasets to urban application. *ISPRS Journal of Photogrammetry and Remote Sensing* 193, 164-186.

Van Coillie, F.M.B., Gardin, S., Anseel, F., Duyck, W., Verbeke, L.P.C., De Wulf, R.R., 2014. Variability of operator performance in remote-sensing image interpretation: the importance of human and external factors. *International Journal of Remote Sensing* 35, 754-778.

Volpi, M., Tuia, D., 2016. Dense semantic labeling of subdecimeter resolution images with convolutional neural networks. *IEEE Transactions on Geoscience and Remote Sensing* 55, 881-893.

Wang, H., Jiang, X., Ren, H., Hu, Y., Bai, S., 2021. SwiftNet: Real-Time Video Object Segmentation, *Proceedings of the IEEE/CVF Conference on Computer Vision and Pattern Recognition* 1296-1305.

Wang, J., Sun, K., Cheng, T., Jiang, B., Deng, C., Zhao, Y., Liu, D., Mu, Y., Tan, M., Wang, X., 2020. Deep high-resolution representation learning for visual recognition. *IEEE transactions on pattern analysis and machine intelligence* 43, 3349-3364.

Wang, L., Li, R., Duan, C., Zhang, C., Meng, X., Fang, S., 2022a. A novel transformer based semantic segmentation scheme for fine-resolution remote sensing images. *IEEE Geoscience and Remote Sensing Letters* 19, 1-5.

Wang, L., Li, R., Zhang, C., Fang, S., Duan, C., Meng, X., Atkinson, P.M., 2022b. UNetFormer: A UNet-like transformer for efficient semantic segmentation of remote sensing urban scene imagery. *ISPRS Journal of Photogrammetry and Remote Sensing* 190, 196-214.

Wang, W., Dai, J., Chen, Z., Huang, Z., Li, Z., Zhu, X., Hu, X., Lu, T., Lu, L., Li, H., Wang, X., Qiao, Y., 2023a. InternImage: Exploring Large-Scale Vision Foundation Models With Deformable Convolutions, *Proceedings of the IEEE/CVF Conference on Computer Vision and Pattern Recognition* 14408-14419.

Wang, W., Tan, X., Zhang, P., Wang, X., 2022c. A CBAM Based Multiscale Transformer Fusion Approach for Remote Sensing Image Change Detection. *IEEE Journal of Selected Topics in Applied Earth Observations and Remote Sensing* 15, 6817-6825.

Wang, X., Yan, X., Tan, K., Pan, C., Ding, J., Liu, Z., Dong, X., 2023b. Double U-Net (W-Net): A change detection network with two heads for remote sensing imagery. *International Journal of Applied Earth Observation and Geoinformation* 122, 103456.

Wu, C., Du, B., Zhang, L., 2023. Fully Convolutional Change Detection Framework With Generative Adversarial Network for Unsupervised, Weakly Supervised and Regional Supervised Change Detection. *IEEE Transactions on Pattern Analysis and Machine Intelligence* 45, 9774-9788.

Wu, Y., Zhang, P., Wu, J., Li, C., 2021. Object-Oriented and Deep-Learning-Based High-Resolution Mapping from Large Remote Sensing Imagery. *Canadian Journal of Remote Sensing* 47, 396-412.

Xie, E., Wang, W., Yu, Z., Anandkumar, A., Alvarez, J.M., Luo, P., 2021. SegFormer: Simple and efficient design for semantic segmentation with transformers. *Advances in Neural Information Processing Systems* 34, 12077-12090.

Xing, Y., Zhang, Y., He, H., Zhang, X., Zhang, Y., 2023. Pansharpening via Frequency-Aware Fusion Network with Explicit Similarity Constraints. *IEEE Transactions on Geoscience and Remote Sensing*.

Xu, J., Luo, C., Chen, X., Wei, S., Luo, Y., 2021. Remote Sensing Change Detection Based on Multidirectional Adaptive Feature Fusion and Perceptual Similarity. *Remote Sensing* 13, 3053.

Xu, S., Dimasaka, J., Wald, D.J., Noh, H.Y., 2022. Seismic multi-hazard and impact estimation via causal inference from satellite imagery. *Nature Communications* 13, 7793.

Yang, J., Du, B., Zhang, L., 2023. From center to surrounding: An interactive learning framework for hyperspectral image classification. *ISPRS Journal of Photogrammetry and Remote Sensing* 197, 145-166.

Yang, Y., Yuan, G., Li, J., 2024. SFFNet: A Wavelet-Based Spatial and Frequency Domain Fusion Network for Remote Sensing Segmentation. *arXiv*.

Yu, Z., Ciais, P., Piao, S., Houghton, R.A., Lu, C., Tian, H., Agathokleous, E., Kattel, G.R., Sitch, S., Goll, D., 2022. Forest expansion dominates China's land carbon sink since 1980. *Nature communications* 13, 5374.

Yuan, Q., Shen, H., Li, T., Li, Z., Li, S., Jiang, Y., Xu, H., Tan, W., Yang, Q., Wang, J., Gao, J., Zhang, L., 2020. Deep learning in environmental remote sensing: Achievements and challenges. *Remote Sensing of Environment* 241, 111716.

Yuan, Y., Fu, R., Huang, L., Lin, W., Zhang, C., Chen, X., Wang, J., 2021. Hrformer: High-resolution vision transformer for dense predict. *Advances in Neural Information Processing Systems* 34, 7281-7293.

Yuan, Z., Hao, C., Zhou, R., Chen, J., Yu, M., Zhang, W., Wang, H., Sun, X., 2023. Efficient and Controllable Remote Sensing Fake Sample Generation Based on Diffusion Model. *IEEE Transactions on Geoscience and Remote Sensing*.

Zhang, C., Harrison, P.A., Pan, X., Li, H., Sargent, I., Atkinson, P.M., 2020a. Scale Sequence Joint Deep Learning (SS-JDL) for land use and land cover classification. *Remote Sensing of Environment* 237, 111593.

Zhang, C., Yue, P., Tapete, D., Jiang, L., Shangguan, B., Huang, L., Liu, G., 2020b. A deeply supervised image fusion network for change detection in high resolution bi-temporal remote sensing images. *ISPRS Journal of Photogrammetry and Remote Sensing* 166, 183-200.

Zhang, R., Zhang, H., Ning, X., Huang, X., Wang, J., Cui, W., 2023a. Global-aware siamese network for change detection on remote sensing images. *ISPRS Journal of Photogrammetry and Remote Sensing* 199, 61-72.

Zhang, X., Cheng, S., Wang, L., Li, H., 2023b. Asymmetric Cross-Attention Hierarchical Network Based on CNN and Transformer for Bitemporal Remote Sensing Images Change Detection. *IEEE Transactions on Geoscience and Remote Sensing* 61, 1-15.

Zhao, H., Shi, J., Qi, X., Wang, X., Jia, J., 2017. Pyramid Scene Parsing Network, 2017

IEEE Conference on Computer Vision and Pattern Recognition (CVPR)6230-6239.

Zhao, S., Zhang, X., Xiao, P., He, G., 2023. Exchanging Dual-Encoder–Decoder: A New Strategy for Change Detection With Semantic Guidance and Spatial Localization. *IEEE Transactions on Geoscience and Remote Sensing* 61, 1-16.

Zheng, S., Wu, Z., Xu, Y., Wei, Z., 2023. Instance-Aware Spatial-Frequency Feature Fusion Detector for Oriented Object Detection in Remote-Sensing Images. *IEEE Transactions on Geoscience and Remote Sensing* 61, 1-13.

Zheng, X., Huan, L., Xia, G.-S., Gong, J., 2020. Parsing very high resolution urban scene images by learning deep ConvNets with edge-aware loss. *ISPRS Journal of Photogrammetry and Remote Sensing* 170, 15-28.

Zhou, W., Newsam, S., Li, C., Shao, Z., 2018. PatternNet: A benchmark dataset for performance evaluation of remote sensing image retrieval. *ISPRS journal of photogrammetry and remote sensing* 145, 197-209.

Zhuoran, S., Mingyuan, Z., Haiyu, Z., Shuai, Y., Hongsheng, L., 2021. Efficient Attention: Attention with Linear Complexities, 2021 IEEE Winter Conference on Applications of Computer Vision (WACV). IEEE3530-3538.

Zou, X., Li, K., Xing, J., Zhang, Y., Wang, S., Jin, L., Tao, P., 2023. DiffCR: A Fast Conditional Diffusion Framework for Cloud Removal from Optical Satellite Images. *arXiv*.

Zou, X., Li, K., Xing, J., Zhang, Y., Wang, S., Jin, L., Tao, P., 2024. DiffCR: A Fast Conditional Diffusion Framework for Cloud Removal From Optical Satellite Images. *IEEE Transactions on Geoscience and Remote Sensing* 62, 1-14.